Published in final edited form as:

*Mol Cell*. 2022 November 17; 82(22): 4307–4323.e10. doi:10.1016/j.molcel.2022.10.003.

# Structure and functionality of a multimeric human COQ7:COQ9 complex

**Mateusz Manicki**[1,2,14], **Halil Aydin**[3,4,14], **Luciano A. Abriata**[5,6,7], **Katherine A. Overmyer**[2,8,9], **Rachel M. Guerra**[1,2], **Joshua J. Coon**[2,8,9,10], **Matteo Dal Peraro**[5,7], **Adam Frost**[3,11,*], **David J. Pagliarini**[1,2,12,13,15,*]

[1]Department of Cell Biology and Physiology, Washington University School of Medicine, St. Louis, MO 63110, USA

[2]Morgridge Institute for Research, Madison, WI 53715, USA

[3]Department of Biochemistry and Biophysics, University of California, San Francisco, San Francisco, CA 94158, USA

[4]Department of Biochemistry, University of Colorado Boulder, Boulder, CO 80309, USA

[5]Institute of Bioengineering, School of Life Sciences, École Polytechnique Fédérale de Lausanne, CH-1015 Lausanne, Switzerland

[6]Protein Production and Structure Core Facility, School of Life Sciences, École Polytechnique Fédérale de Lausanne, CH-1015 Lausanne, Switzerland

[7]Swiss Institute of Bioinformatics, CH-1015 Lausanne, Switzerland

[8]National Center for Quantitative Biology of Complex Systems, Madison, WI 53562, USA

[9]Department of Biomolecular Chemistry, University of Wisconsin–Madison, Madison, WI 53562, USA

[10]Department of Chemistry, University of Wisconsin-Madison, Madison, WI 53506, USA

[11]Chan Zuckerberg Biohub and Altos Labs Bay Area Institute of Science, San Francisco, CA, USA

[12]Departament of Biochemistry and Molecular Biophysics, Washington University School of Medicine, St. Louis, MO 63110, USA

[*]Corresponding authors' afrost@altoslabs.com; pagliarini@wustl.edu.

AUTHOR CONTRIBUTIONS

**Mateusz Manicki:** Conceptualization, Methodology, Formal analysis, Investigation, Writing – original draft, Writing – review and editing, Visualization, Project Administration. **Halil Aydin:** Conceptualization, Methodology, Software, Formal analysis, Investigation, Data curation, Writing – review and editing. **Luciano A. Abriata:** Conceptualization, Methodology, Software, Formal analysis, Investigation, Data curation, Writing – review and editing, Visualization. **Katherine A. Overmyer:** Methodology, Formal analysis, Investigation, Data curation. **Rachel M. Guerra:** Conceptualization, Methodology, Writing – review and editing. **Joshua J. Coon:** Supervision, Funding acquisition. **Matteo Dal Peraro:** Methodology, Writing – review and editing, Supervision, Funding acquisition. **Adam Frost:** Conceptualization, Methodology, Writing – review and editing, Supervision, Funding acquisition. **David J. Pagliarini:** Conceptualization, Methodology, Writing – review and editing, Supervision, Project administration, Funding acquisition.

DECLARATION OF INTERESTS

J.J.C. is a consultant for Thermo Scientific. A.F. is a shareholder and employee of Altos Labs and a shareholder and consultant for Relay Therapeutics, LLC.

[13]Departament of Genetics, Washington University School of Medicine, St. Louis, MO 63110, USA

[14]These authors contributed equally: Mateusz Manicki, Halil Aydin

[15]Lead Contact

## SUMMARY

Coenzyme Q (CoQ) is a redox-active lipid essential for core metabolic pathways and antioxidant defense. CoQ is synthesized upon the mitochondrial inner membrane by an ill-defined 'complex Q' metabolon. Here we present structure-function analyses of a lipid-, substrate-, and NADH-bound complex comprised of two complex Q subunits: the hydroxylase COQ7 and the lipid-binding protein COQ9. We reveal that COQ7 adopts a ferritin-like fold with a hydrophobic channel whose substrate-binding capacity is enhanced by COQ9. Using molecular dynamics, we further show that two COQ7:COQ9 heterodimers form a curved tetramer that deforms the membrane, potentially opening a pathway for the CoQ intermediates to translocate from the bilayer to the proteins' lipid-binding sites. Two such tetramers assemble into a soluble octamer with a pseudo-bilayer of lipids captured within. Together, these observations indicate that COQ7 and COQ9 cooperate to access hydrophobic precursors within the membrane and coordinate subsequent synthesis steps toward producing CoQ.

### Keywords

Coenzyme Q; quinone biosynthesis; COQ7; COQ9; Protein-lipid complex; mitochondria; diiron proteins; protein-membrane interaction

## INTRODUCTION

Quinones are central to energy transducing systems in organisms across all kingdoms of life (Schoepp-Cothenet et al., 2013). Many of the quinones essential for biology are attached to hydrophobic moieties that keep them sequestered within membranes. Within the bilayer, they participate in electron transfer between proteins involved in diverse processes, including respiratory and photosynthetic complexes (Nowicka and Kruk, 2010, Liu and Lu, 2016). Despite their profound roles in life, many aspects of quinone biosynthesis and trafficking remain undefined (Stefely and Pagliarini, 2017, Kemmerer et al., 2021).

Coenzyme Q (CoQ, ubiquinone) is a quinone found within every eukaryotic membrane (Turunen et al., 2004) and that is best known for its role in the mitochondrial electron transport chain (Crane, 2007). CoQ comprises a redox-active head group that can carry electrons and an extremely hydrophobic isoprenoid tail that drives its partitioning into the hydrophobic core of the bilayer. In eukaryotes, the head group precursor is derived from aromatic amino acids and imported into mitochondria where it becomes prenylated. The head group is then chemically modified by several enzymes, each of which must access intermediates buried within the membrane (Stefely and Pagliarini, 2017). Interestingly, individual intermediates of the pathway are difficult to detect, suggesting that substrate channeling might occur between the biosynthetic enzymes (COQ proteins). Supporting this,

recent work has begun to define a dynamic complex of COQ proteins (complex Q, or CoQ-synthome) that may act as a metabolon (Subramanian et al., 2019, Floyd et al., 2016, He et al., 2014).

Due in part to its dynamic nature—and the fact that structural information on multiple individual COQ proteins has not been reported—complex Q has evaded detailed structural and biochemical characterization. Protein interaction maps in *Saccharomyces cerevisiae* and human cells, however, suggest the complex is comprised of at least seven proteins (COQ3, COQ4, COQ5, COQ6, COQ7, COQ8, COQ9) (Szklarczyk et al., 2020, Allan et al., 2015, Guo et al., 2017). The architecture and subunit stoichiometry remain unknown, as does whether discrete sub-complexes exist. However, observations in yeast (Lohman et al., 2014), mice (García-Corzo et al., 2013), and humans (Danhauser et al., 2016) have shown that a direct physical and functional relationship exists between COQ7, an iron-dependent hydroxylase, and COQ9, a lipid-binding auxiliary protein, and that mutations in either protein lead to the accumulation of the penultimate CoQ intermediate, demethoxy-coenzyme Q (DMQ). Mutations of these proteins result in neurological defects, decreased activity of the mitochondrial electron transport chain, reduced levels of ATP synthesis, and increased mitochondrial oxidative stress (Danhauser et al., 2016, Smith et al., 2018, Kwong et al., 2019, Duncan et al., 2009, Olgac et al., 2020, Wang et al., 2017, Freyer et al., 2015, Wang et al., 2015).

Details of COQ7 and COQ9 cooperation are not well understood. Recently, we demonstrated that COQ9 is a membrane-binding protein capable of selectively engaging aromatic isoprene lipids (Lohman et al., 2019). This observation suggested that COQ9 could assist COQ7 in membrane association and/or in accessing a CoQ intermediate. However, it is still unclear how COQ proteins surmount hydrophobic barriers to access CoQ intermediates, which are expected to predominantly reside within the bilayer. To explore these ideas, we co-expressed and co-purified an unexpected octameric COQ7:COQ9 complex, solved its atomic structure using cryo-EM, and explored its function experimentally and computationally.

## RESULTS

### Cryo-EM structure of human COQ7

COQ7 is a membrane-bound di-iron protein and an enigmatic member of the ferritin family that has been recalcitrant to experimental structural characterization (Jonassen et al., 1998, Behan and Lippard, 2010, Andrews, 2010). Here, using an *E. coli* expression system, we co-expressed human COQ7 (residues 39–217 with N-terminal GB1 tag (Huth et al., 1997)) together with its native partner, human COQ9 (residues 79–318 with an N-terminal His tag), and performed metal affinity and gel filtration chromatography. Our results revealed that COQ7 and COQ9 co-purify as a 1:1 complex with a molecular weight of ~240 kDa, suggestive of an octamer (Figures 1A and S1A–D). Further characterization by TEM confirmed the homogeneity of the sample and revealed monodispersed particles of the intact COQ7:COQ9 complexes with striking symmetry (Figure S1E, S1F).

The complex was vitrified, imaged, and reconstructed using 3D single-particle cryo-EM analysis. An initial density map reached ~3.5Å but was incompletely occupied by the known cofactor NADH (Figure S2, S3 and Table 1). We therefore incubated the COQ7:COQ9 hetero-octamers with excess NADH prior to vitrification. This second dataset yielded an improved map at an overall nominal resolution of ~2.4 Å, with D2 symmetry, and robust density for NADH (Figure S4, S5, and Table 1). Most of the side chains were well-resolved and allowed *de novo* atomic model building of COQ7 and COQ9, with the exception of the flexible N-terminal GB1 tag on COQ7 and C-terminal $10^{th}$ α-helix of COQ9 (Figure S6 and Table 1).

COQ7 has a rod-shaped structure (Figure 1B) with approximate dimensions of 45 Å X 30 Å X 27 Å and shares structural similarity with bacterioferritin (~1.7 Å r.m.s.d. over 173 Cα atoms of COQ7) (Figure S7A). However, major structural changes are apparent and suggest that the fold was repurposed from the classic iron-storing ferritin to a membrane-binding hydroxylase (Figure S7B). The overall structure is comprised of six α-helices (α1- α6) (Figure 1B). Helices α1, α2, α4, and α5 exhibit a compact four-helix bundle containing residues properly oriented to bind two metal ions (Fe1 and Fe2) and form the di-iron active site (Figure S7C). The three-dimensional map of COQ7 presents the atomic coordinates of the conserved and functionally important iron coordination motif (E-($X_6$)-Y-($X_{22}$)-E-($X_2$)-H-($X_{48}$)-E-($X_6$)-Y-($X_{28}$)-E-($X_2$)-H) (Figure S7D). While the protein chains were well defined by electron density, we did not observe density for the active site ions and could only estimate their position by homology. By analogy with bacterioferritin, the first metal ion binding site, Fe1, would be coordinated by E60, H93, Y149, and E178, whereas the Y67, E90, E142, and H181 residues would coordinate the Fe2 site.

In addition to the four-helix bundle, the COQ7 structure contains a short helix (α3) and a C-terminal helix (α6) that is connected to the rest of the molecule via a long loop. These features represent a novel organization for ferritin-like di-iron carboxylate enzymes (Figure S7E). The helices α3 and α6 contribute to the formation of a large hydrophobic channel along with α1 and α4 (Figures 1B and S7F), and a flat hydrophobic surface on the membrane-proximal side of the protein (Figure 1C). The residues L111, L114, L118, L122, I202, V209, L213, and L217 define the outer entrance to the channel, whereas the inner surface is lined by A63, I66, W115, V141, I145, I203, C207, A210, and I211. The apparent channel seems sufficiently large to admit entry of quinone intermediates and access to the di-iron center. Consistently, alternative oxidases (AOX), which use CoQ as a substrate, display a similar structural feature (Figure S7G–I) (Moore et al., 2013). Furthermore, we observed a clearly defined isoprenoid quinone-like density extending from the inner surface of the hydrophobic channel (Figures 1D and S6D).

Within COQ7's hydrophobic channel, the quinone head group fits comfortably into the hydrophobic pocket and the isoprene tail adopts a U-shaped conformation that is stabilized by conserved hydrophobic residues (L118, A121, L122, L129, L199, and I202) located on the protein surface. To determine the identity of this isoprenoid, we performed liquid chromatography with tandem mass spectrometry (LC-MS/MS) of the purified COQ7:COQ9 complex and bacterial cells used for its production. The protein sample showed 50x enrichment (~20% of total lipid signal) for octaprenylphenol (OPP), a bacterial CoQ

biosynthetic intermediate (Aussel et al., 2014) (Figure 1E). In agreement with the logic of biosynthetic pathways, no enrichment of $CoQ_8$ (the *E. coli* version of CoQ) was detected (Figure 1F). Together, these results identify OPP as the bacterial ubiquinone intermediate occupying the hydrophobic channel leading to the active site of COQ7.

To validate our observations, we turned to *S. cerevisiae*, which can survive without CoQ under fermentative growth conditions but require it for respiration. Structural features and evolutionary conservation of COQ7 (Figure S8B) guided us in the design of mutations that should block the hydrophobic channel. As expected, mutations G123Y, M127W, I219Y, I222Y, or A226Y (corresponding to human L118, L122, I203, G206, or A210 residue) that introduce a large hydrophobic residue into the channel, reduced $CoQ_6$ levels in yeast and their ability to respire (Figure 1G,1H) without affecting the proteins' stability as judged by expression levels (Figure 1I). To confirm disruption of Coq7 function in the mutants, we used MS to measure levels of $DMQ_6$, the *bona fide* substrate of Coq7. In all cases, we detected $DMQ_6$ showing that upstream steps of $CoQ_6$ biosynthesis are at least partially functional (Figure 1J). Of note, the structure clarifies the deleterious effects of COQ7 mutations found in human patients, including a recent case of K200fs56 mutation[17] that localizes to COQ7's $6^{th}$ helix revealed in this manuscript (Figure S7J).

## Cryo-EM reveals details of NADH binding by COQ7

To achieve their enzymatic activity, di-iron proteins require a reduction of their active site iron atoms from $Fe^{3+}$ to $Fe^{2+}$ (Jasniewski and Que, 2018). *In vitro*, quinone substrates can mediate the transfer of electrons from NADH to COQ7's active site (Lu et al., 2013). Comparison of our unsoaked and NADH-soaked reconstructions showed how NADH binds to every protomer of COQ7 (Figure 2A and S8A) via a set of evolutionarily conserved and surface-exposed residues (Figure S8B) without inducing global conformational changes. Although it is unknown how hydride is transferred from NADH to the protein, sequential electron-proton-electron donation has been proposed to involve COQ7's amino acid triad E60/H148/Y149(Lu et al., 2013) (Behan and Lippard, 2010). In our structure, NADH localizes next to a water-filled channel formed by this triad and is close enough to the active site pocket (~15 Å) to permit tunneling of charges to the expected quinone acceptor (Gray and Winkler, 2003, Gray and Winkler, 2005, Moser et al., 1992, Hammes-Schiffer and Stuchebrukhov, 2010) (Figures 2B, 2C and S9A–E). This positioning of NADH is provided by the R51, R208, Y212, and R216 residues of COQ7 (Figure 2D). Interestingly, the interaction between R208 and NADH is bridged by the headgroup of a clearly visible, but unidentified, phospholipid molecule (Figure 2D), suggesting a functional role for membrane lipids in the stabilization of NADH contacts.

To test the functional importance of the identified residues, we purified COQ7 alongside a quadruple $COQ7^{R51A/R208A/Y212A/R216A}$ mutant (Figure S9F) and tested their activity *in vitro* by measuring the loss of NADH fluorescence upon its oxidation to NAD+. In agreement with its proposed mechanism of action, wild type COQ7 slowly oxidized NADH and transferred electrons to a quinone acceptor, changing its redox state as measured by an HPLC equipped with a redox-sensitive electrochemical detector (HPLC-ECD) (Figure S9G–J). However, the mutant markedly lost activity (Figures 2E, 2F and S9G–J).

Next, we again sought to validate the importance of our observations *in vivo* using the yeast respiration system. High overexpression of $Coq7^{R54A}$ or $Coq7^{R224A}$ point mutants (corresponding to residues R51 and R208 in human COQ7, respectively) was not able to fully support $CoQ_6$ production or respiratory growth. Interestingly, mutants W228A and R232A (Y212 and R216 in humans) showed only a minor $CoQ_6$ reduction, and hence fully supported respiration (Figure 2G–I). In the presence of high (100 μM) 4-hydroxybenzoate (4-HB), the cytosolic CoQ precursor, only the quadruple mutant exhibited significantly reduced $DMQ_6/CoQ_6$ levels, presumably because overexpression of the single mutants was sufficient to drive $CoQ_6$ production under these conditions (Figure S9K–M). Alternatively, given that the purpose of the NADH activity of Coq7 is only to support reduction of the $DMQ_6$ substrate, this function might largely be dispensable if upstream pathway enzymes or other oxidoreductases are capable of generating $DMQ_6$. Nonetheless, the partial loss of the *in vitro* activity of the quadruple human COQ7 mutant and the reduced levels of $CoQ_6$ in yeast mutants indicate that the NADH's positioning observed in cryo-EM is biologically relevant. Furthermore, a recent manuscript (Wang et al., 2022) reports that mutation of R54—one of the NADH-binding residues that tested here—causes primarily neuromuscular pathology in humans.

## Cryo-EM reveals lipid molecules bound to the COQ7:COQ9 heterodimer.

Efficient interaction of COQ7 with COQ9 is known to be essential for CoQ production *in vivo.* We previously described the crystal structure and lipid-binding activity of human COQ9 and used molecular dynamics simulations to predict its interaction with a COQ7 homology model on a lipid membrane (Lohman et al., 2019). Here, using cryo-EM, we determined the structure of the complex bound to lipids and discovered an unexpected higher-order oligomer.

The atomic structure of human COQ9 includes helices α1-α9 and fits well as a rigid body to the density of the COQ7:COQ9 complex (R.M.S.D = 0.95 Å) with the α7- α8 loop found in only one of the two conformations present in the isoprene-bound crystal structure of COQ9 (PDB: 6DEW). The lack of the $10^{th}$ helix suggests that it does not have a well-defined position, consistent with its role in the initial recognition of the lipid membrane.

The overall architecture of the COQ7:COQ9 heterodimer is shown in Figure 3A. We observed an interface that is stabilized by several hydrogen bonds, hydrophobic interactions, and an intermolecular salt bridge between COQ9 (D225, D226, T236, D237, F238, W240, and Y241) and COQ7 (N98, M101, V102, R105, R107, P108, T109, V110, and M112) residues (Figure 3B). Notably, this limited contact interface between COQ7 and COQ9 may not be sufficient for stable complex formation. Consistently, a single point mutation in that region $COQ9^{W240K}$ led to total disruption of the octameric 240 kDa COQ7:COQ9 complex and formation of a smaller ~55 kDa complex comprised only of COQ9 (Figures 3C and S10A–C).

Investigation of the 2.4 Å cryo-EM density map revealed multiple lipid-like densities engaged with the surface of the proteins. They were not randomly oriented, but rather formed a 30 Å tall, bilayer-like, warped sheet with lipid tails pointing towards each other and the headgroups pointing in opposite directions (Figure 3D, 3E). Our lipidomics results

suggest the lipids likely originate from *E. coli* plasma membrane (Sohlenkamp and Geiger, 2016, Morein et al., 1996) (Figure S10D). These observations may have biological relevance because quinones are known to be trapped within cellular membranes. Due to their extreme hydrophobicity, these molecules cannot transverse through the headgroup layer (Kaurola et al., 2016, Teixeira and Arantes, 2019, Katsikas and Quinn, 1983, Hauß et al., 2005, Ausili et al., 2008, Fato et al., 1986) and thus are likely extracted by the COQ7:COQ9 complex.

We previously determined the crystal structure of COQ9 with an isoprenoid substrate and identified a lipid-binding pocket inside the protein. In the cryo-EM structure, this pocket is located between the displaced lipid headgroups, consistent with a model whereby COQ9 binding reorganizes the membrane to enable access to its interior. Interestingly, we did not observe a well-defined density for lipids resembling CoQ intermediates within the lipid-binding cavity of COQ9 (Figure 3F), which could indicate that the quinone molecule was transferred to COQ7. If so, then COQ7 should be enriched in OPP when in complex with COQ9. To test this, we measured quinone content in COQ7 and COQ9 purified alone and as a complex. As expected, we observed a higher OPP level in the COQ7:COQ9 complex than in COQ7 or COQ9 alone (Figures 3G and S10E). Knowing there is no observable OPP bound to COQ9 in the COQ7:COQ9 complex, the higher OPP signal most likely represents an increased level of OPP bound to COQ7 due to COQ9's actions. Together, our structural model advances our previous *in vitro* analyses by defining COQ7-COQ9-lipid interactions likely critical for ubiquinone synthesis and trafficking.

## COQ7 and COQ9 may exist as a heterotetramer

In the cryo-EM structure, two heterodimers of COQ7:COQ9 come together on the same side of the lipid pseudo-bilayer and form a curved tetramer with a hydrophobic surface suitable for membrane interaction. Viewed from the membrane surface, one heterotetrameric assembly is approximately 100 Å in diameter and 40 Å axially with a solvent-exposed central pore that accommodates one NADH molecule (Figure 4A). This NADH likely can bind in two symmetrical orientations so that the charge-donating nicotinamide ring can support activity of every COQ7 protomer. The pore is formed by two COQ7:COQ9 heterodimers that make additional contacts with an interface that buries around 261 $Å^2$ of surface area. The N-terminal segment of the α7 helix region of COQ9 and α6 helix of COQ7 from opposing heterodimers associate around a 2-fold axis normal to the membrane plane, with most the intimate contacts occurring between COQ9 residues L209, P210, and H211 and COQ7 residues S201, Q204, A205, and R208 (Figure 4B).

To test the importance of this region, we generated corresponding yeast mutants and measured their $CoQ_6$ levels and ability to respire. We observed that mutations of P210 and S201—represented by $Coq9^{P155R}$ and $Coq7^{E217R}$ in yeast—led to impaired respiration and diminished $CoQ_6$ levels, despite high expression levels of the mutated proteins (Figure 4C–E). These mutated yeast displayed moderate respiratory growth over time indicating that the proteins remain at least partially functional. Despite the magnitude of the $Coq9^{P155R}$ phenotype, disruption of this proline was insufficient to prevent formation of the 240 kDa complex (Figure S10F), suggesting that lipids also contribute to the stability of the COQ7-

COQ9 interaction. Due to the large hydrophobic surfaces present in COQ7 and COQ9, we hypothesize that membrane association may also play a role in their stabilization.

### MD simulations of the tetramer engaging and reshaping a membrane

To explore whether and how the tetrameric form binds the lipid bilayer to potentially facilitate modification of the embedded quinone substrate, we performed atomistic molecular dynamics (MD) simulations on systems set up with the COQ7:COQ9 heterotetramer manually placed with its hydrophobic surface near but not binding a model membrane enriched with $DMQ_{10}$ at ~4% molar concentration. As the flexible $10^{th}$ helix of COQ9 was not observed by cryo-EM, we modeled it based on our crystal structure (PDB: 6AWL). The systems were parametrized as described in Methods, and we ran four independent replicas of this simulation starting with different seeds, all for 1.2–1.6 μs.

In the simulations, the tetrameric arrangement inferred from the cryo-EM structure rapidly (<50 ns) bound the membrane. The interaction remained stable for the duration of the simulation (over 1 μs, Figure 5A) and entailed no major conformational changes in the core of the tetramer. The peripheral $10^{th}$ helix of COQ9 remained flexible. Upon membrane binding, COQ7 and COQ9 progressively gained direct access to the hydrophobic portion of the lipid bilayer (Figure 5A).

Following membrane association, we observed nearby lipids tilt away from a normal bilayer architecture until they resembled the angular orientations of the lipids we resolved in the cryo-EM density map. In addition, the lipids concentrated their headgroups on the periphery of the protein-membrane contact region to form a rim around the membrane-facing surface of the tetramer (Figure 5B). As a result of this interaction, the membrane became deformed by ~10 to 20 Å into a funnel-like shape with proteins located at its bottom (Figures 5A, 5C and S11A, S11B), and the DMQ molecules clustered around the proteins in high density (Figures S11C, S11D). This remodeling of the membrane exposed the carbon-tail region of its lipids directly to hydrophobic surfaces of COQ7 and COQ9 and permitted their interaction with the locally concentrated pool of DMQ (Figures 5B and S11C–E). At the same time, peripheral interactions with cardiolipin around the hydrophobic interior anchored the protein complex to the membrane (Figure S11C).

We note that despite the high density of DMQ around the membrane-facing surfaces of COQ7 and COQ9, we observed no molecule docking into any active site, not even the one we observed populated with OPP (Figure S11E). Such entry may require conformational changes of COQ7 and/or COQ9 that are unlikely to occur in ~1 microsecond-long atomistic simulations. To explore possible substrate entry and exit routes and accompanying conformational changes, we devised a reverse computational experiment in which we monitored exit of a quinone from COQ7. We chose $CoQ_{10}$ as a bulkier proxy of COQ7's product (DMQ), placed it in position of the OPP molecule observed in the cryo-EM map, and monitored its release. Replica-exchange simulations were impossible to tune, as they resulted in membrane disruption. We therefore tested regular simulations at various stable temperatures. At the elevated temperature of 450K, we observed the docked $CoQ_{10}$ dissociate from COQ7 without compromising the protein or membrane stabilities within the simulated timescale (~1–1.5 microsecond).

Out of 10 replicas at 450K, we observed $CoQ_{10}$ leaving the active site in two directions: eight times directly towards and into the membrane bulk, and twice towards COQ9 before moving to the membrane bulk (Figures 5D and S11F). In every case, release of the ligand involved a displacement of the two COQ7 helices (α3, α6) that form the hydrophobic channel leading to the active site, temporarily widening its opening towards the membrane.

Although it is possible that some of our observations are due to the high temperatures used to promote unbinding, we noticed that residue W115 of COQ7 flips rotameric conformation repeatedly (Figure 5E) within the pathway where the $CoQ_{10}$ molecule moves towards COQ9 (Figure 5F). This is realized through rotation of the Chi1 angle (Figure 5G) in concert with separation of the two helices represented by the increase of the distance between W115's and A210's Cα atoms (Figure 5H). Once the small molecule has left the active site, W115's sidechain flips to a second stable conformation where the indole ring fills the space that the headgroup of $CoQ_{10}$ was occupying (Figure 5F,5H). We thus postulate that residue W115 could act as a gate for a potential pathway of substrate entry from an initial binding site around COQ9 into the active site at COQ7, and possibly also modulate separation of COQ7's helices to allow release of the product towards the membrane.

To test the relevance of this tryptophan experimentally, we mutated the corresponding W120 residue in yeast. Substitution with much smaller but also hydrophobic methionine decreased $CoQ_6$ levels (Figure 5I) and compromised respiration (Figure 5J), but mostly preserved levels of the Coq7's *bona fide* substrate $DMQ_6$ (Figure 5K). The high expression level of the mutant (Figure 5L) indicates that the Trp residue is indeed important for the function of COQ7 and not its stability. Accordingly, substitution of W120 in yeast with histidine, which also contains an aromatic ring but is more polar than the tryptophan, also distorted the production of $CoQ_6$ (Figure 5I–L).

## The overall COQ7:COQ9 complex forms a hetero-octameric cage.

Physiologically, COQ proteins are associated with the matrix side of the inner mitochondrial membrane (Morgenstern et al., 2017, Vögtle et al., 2017) where they can interact with each other to produce CoQ. The single-leaflet-binding heterotetrameric COQ7:COQ9 fits well into this model. However, the cryo-EM revealed that the purified COQ7:COQ9 complex forms a soluble ~240 kDa capsid-like octamer composed of two "closed" heterotetramers (Figures 6A and S12A–D). The functional significance of this assembly state remains unclear.

Globally, the octamer resembles a cube with a proteinaceous outer shell, a middle layer of protein-interacting lipids, and an inner core consisting of clearly visible lipid-like densities. Our MS lipid analyses revealed that highly abundant phospholipid species in *E. coli* copurified with recombinantly expressed COQ7 and COQ9 (Figure S10D). When considered with the structure (Figure 3D), and the simulations of membrane binding (Figure 5A), these results suggest that lipids shield the hydrophobic surfaces of the proteins and therefore assist solubility and stability (Figure 6B).

To test this notion, we delipidated the sample and monitored soluble complex concentrations using SDS-PAGE. We observed 33% protein loss upon 1h incubation (Figure 6C) without

the appearance of any new oligomeric structures (Figure 6D). This indicates that protein-lipid interactions are important for the stability of the COQ7:COQ9 complexes isolated from *E. coli*. In addition, we asked if protein-protein interactions also have a stabilizing effect. We performed thermal denaturation assays to measure the stability of the lipid-rich but individually purified COQ7, COQ9, COQ7 and COQ9 combined *in vitro*, and the COQ7:COQ9 complex. The $T_m$ of the wild-type COQ9 and COQ7 were 49.1 °C and 62.7 °C, respectively. Mixing of the proteins increased the melting temperature to 66.8°C, which shows that COQ proteins are strongly stabilized by direct interactions *in vitro*. The melting temperature of the purified COQ7:COQ9 complex was higher (71.6°C), possibly representing a more optimal organization of lipids and proteins in the complex (Figure 6E).

The octameric structure of the COQ7:COQ9 complex with the membrane trapped inside sparks intriguing ideas about its potential roles, for example as a lipid/quinone transporter or an enzymatic nano-chamber. Such functional states are rather unexpected, since the preponderance of evidence places COQ proteins only on the matrix face of the IMM (Vögtle et al., 2017, Morgenstern et al., 2017, Hung et al., 2014, Vögtle et al., 2012). However, in human and nematodes COQ7 has been reported to exist also in the nucleus (Monaghan et al., 2015). Although these findings are debated (Liu et al., 2017), they highlight that COQ7 may have additional functions, and thus the COQ7:COQ9 octamer warrants further experimental investigation. Collectively, we conclude that our data argue in favor of the COQ7:COQ9 tetramer being a physiologically-active form of the complex that can engage lipid bilayers and whose formation depends on protein-protein and protein-lipid interactions. The significance of the octameric state remains under investigation.

## DISCUSSION

Quinones are highly reactive molecules (Bolton et al., 2000) that can be produced by cells in the form of lipids and employed as essential redox cofactors for membrane-bound enzymes (Liu and Lu, 2016, Hidalgo-Gutiérrez et al., 2021). However, the biosynthesis of these hydrophobic quinones presents biochemical challenges at the aqueous/membrane interface (Forneris and Mattevi, 2008). Enzymes involved in this biosynthesis require simultaneous access to water-soluble cofactors and lipid-soluble substrates and need to avoid the release of immature precursors into the membrane that may lead to toxic interactions with the quinone-dependent enzymes (Fernández-del-Río et al., 2020). In the CoQ pathway, prenylation occurs at a very early step (Stefely and Pagliarini, 2017). Due to the extremely hydrophobic character of the subsequent intermediates, a number of simulations, and *in vitro* experiments (Kaurola et al., 2016, Galassi and Arantes, 2015, Hauß et al., 2005, Metz et al., 1995, Samorì et al., 1992), we contend that their localization within the lipid bilayer is most expected. Indeed, $DMQ_{10}$ produced in human COQ7 KO cells can partially support activity of the mitochondrial respiratory chain (Wang and Hekimi, 2021), indicating that it must be present inside the membrane to be accessible to the respiratory complexes. How DMQ and other CoQ intermediates are accessed and modified by CoQ proteins is unknown.

In recent years, multiple groups have reported evidence for a complex of CoQ-related biosynthetic proteins (Subramanian et al., 2019, Floyd et al., 2016, Allan et al., 2015, Lohman et al., 2014, Yen et al., 2020, Marbois et al., 2009, Hsu et al., 2000, Hsieh et

al., 2007, Marbois et al., 2005, Tran et al., 2006, Tauche et al., 2008), leading to the speculation that CoQ is produced by a ‘metabolon’ that might surmount these challenges. Indeed, in *E. coli*, multiple proteins in the CoQ pathway form a soluble cytosolic complex that completes a series of enzymatic reactions before returning to membrane (Chehade et al., 2019). Thus far, however, little has been elucidated about the structure and mechanism of the eukaryotic CoQ metabolon whose components associate with the inner mitochondrial membrane (Vögtle et al., 2017, Morgenstern et al., 2017). Here, we offer structural insight into the actions of a COQ protein complex at a lipid bilayer.

Our data support and extend our previous model that COQ9 facilitates substrate delivery to COQ7(Lohman et al., 2019); however, the precise mechanism remains elusive. We demonstrate that the COQ7-COQ9 interaction facilitates binding of the $CoQ_8$ precursor OPP, which was enriched 50-fold over background. We further reveal the structure of COQ7 with two of its helices forming a membrane-interacting hydrophobic surface and a quinone-binding channel leading to the protein’s active site. However, in the conformation captured by cryo-EM, this channel is not oriented towards COQ9 but towards the interior of the lipid bilayer. It is possible that COQ7 may rotate to accept the substrate from COQ9 as part of an overall cooperative mechanism; however, we did not observe this in our molecular dynamics simulations. Instead, in a separate simulation, we observed that the two membrane-bound helices of COQ7 can open and permit lateral quinone movement. Therefore, we speculate that COQ9 partially desorbs the quinone-intermediate from the membrane and stimulates opening of COQ7’s helices to allow a guided lateral diffusion of the intermediate into COQ7. Perhaps, this process is facilitated by a conformational change of the α7-α8 loop (captured in COQ9’s crystal structure PDB: 6DEW) that carries the W240 residue essential for quinone-substrate binding and interaction with COQ7.

We further speculate that the tetrameric form of the COQ7:COQ9 complex creates a proteinaceous boundary that protects intermediates from diffusing away. Interestingly, localization and dynamics of quinones in membranes are known to be influenced by both membrane composition and curvature (Budin et al., 2018, Michaelis and Moore, 1985), in addition to the presence of specific proteins (Singharoy et al., 2019). Therefore, in agreement with our simulations, we also hypothesize that the membrane distortion induced by the COQ7:COQ9 tetramer helps to retain and concentrate the quinone-intermediates close to the membrane surface where they can be efficiently extracted and modified by COQ enzymes.

Although both COQ7 and COQ9 are enriched at a high molecular weight consistent with their incorporation into a full complex Q/CoQ synthome, they are also detected at lower molecular weights (Tran et al., 2006, He et al., 2014). Further studies are required to define what the complexes of different sizes represent. It is possible that complex Q is a singular complex that directly channels quinone-intermediates between its proteins, but that is not sufficiently stable to survive purification. Alternatively, COQ proteins may assemble into smaller complexes that coexist at specific regions of the mitochondrial membrane where they process their substrates. Intriguingly, the stability of COQ proteins and their interactions seems to be positively affected by the presence of CoQ and its intermediates in the membrane (He et al., 2014, Padilla et al., 2008). Moreover, fluorescent microscopy

studies have shown that *in vivo* COQ proteins assemble into CoQ-domains and colocalize with ER-mitochondria contact sites in yeast (ERMES) (Subramanian et al., 2019, Eisenberg-Bord et al., 2019) that facilitate exchange of lipids between the organelles (Acoba et al., 2020). Whether complex Q and CoQ-domains are one entity, and whether local membrane composition regulates CoQ production, remain to be established.

Further work will be also required to elucidate what oligomeric forms of the COQ7:COQ9 complex exist *in vivo*. We suggest the COQ7:COQ9 heterotetramer to be the primary biological unit; however, it cannot be ruled out that other assemblies of COQ7 and COQ9 have biological relevance. It is intriguing that the very stable COQ7:COQ9 octamer is rich in lipids but does not require detergents for purification. How and why two membrane-binding proteins would entrap and solubilize a portion of membrane is entirely unknown. The membrane curving and thinning observed in the cryo-EM and molecular dynamics simulations may indicate full pinching off of a part of the membrane leading to formation of an enzymatic nano-chamber *in vivo*. Interestingly, COQ7 has been suggested to play additional functions in the cell by participating in mtDNA homeostasis (Gorbunova and Seluanov, 2002, Kirby and Patel, 2021) and stress-signaling (Monaghan et al., 2015, Liu et al., 2017). Moreover, *COQ7* (called *CAT5* in yeast) and *YLR202C* (ORF partially overlapping with *COQ9*) were hits in a screen identifying *loci* important for sterol uptake (Reiner et al., 2006). Therefore, roles for COQ7 and COQ9 beyond complex Q, and their existence in different oligomeric forms, are possibilities that will require future studies.

Overall, our results provide molecular insight into how proteins can cooperate at a lipid membrane to selectively extract and process an extremely hydrophobic substrate. Although we focused here on CoQ biosynthesis, we anticipate that our findings will have much broader utility because, in contrast to the COQ7:COQ9 complex that we resolved with a bound layer of lipids, virtually all other structures of peripheral membrane proteins deposited in PDB lack bound phospholipids that could explain how such proteins associate with their target biological membranes.

## LIMITATIONS OF THE STUDY

Although overall consistent, our results do have important limitations. Due to the use of a bacterial system of protein expression, we were unable to retrieve demethoxy-coenzyme Q (DMQ), the established substrate of COQ7. Instead, our structures are occupied by octaprenylphenol (OPP), an early intermediate of $CoQ_8$ production in *E. coli.* Moreover, the OPP molecule is displaced from COQ7's active site by ~10Å, and thus it only marks the route towards the active site. How exactly the quinone substrate travels along that path remains to be elucidated as its exchange between COQ9 and COQ7 was never directly observed in our molecular dynamics simulations. The lack of substrate and iron at the active site prohibits us from making conclusive statements about the catalytic mechanism of COQ7. Unfortunately, iron has very complex coordination chemistry; thus, we are not able to easily overcome this limitation using *in silico* methods. However, we contend that our structure presents a plausible quinone-protein arrangement that will guide more detailed studies in the future.

# STAR METHODS

## RESOURCE AVAILABILITY

**LEAD CONTACT—**Further information and requests for resources and reagents should be directed to and will be fulfilled by the D.J.P (pagliarini@wustl.edu).

**MATERIALS AVAILABILITY—**All unique/stable reagents generated in this study are available from the lead contact upon reasonable request.

### DATA AND CODE AVAILABILITY

- All data were deposited in Cell-Press-recommended, datatype-specific repositories and made publicly accessible.

  The atomic coordinates of NADH-bound COQ7:COQ9 complex and COQ7:COQ9 complex only have been deposited in the Protein Data Bank with accession numbers 7SSS and 7SSP, respectively. All of the 3D cryo-EM density maps associated with this study have been deposited in the Electron Microscopy Data Bank under accession numbers EMD-25413 for NADH-bound COQ7:COQ9 complex and EMD-25412 for COQ7:COQ9 complex only. Accession numbers are also listed in the key resources table.

  The raw LC-MS lipidomics data generated during the current study have been deposited at MassIVE repository and are publicly available under accession code MSV000089931 as of the date of publication. Accession numbers are also listed in the key resources table.

  The raw Western Blot images were deposited at Mendeley Dataset repository under accession code 10.17632/33sjh9gxrm.1. The accession number is also listed in the key resources table.

- This paper does not report original code.
- Any additional information required to reanalyze the data reported in this paper is available from the lead contact upon request.

## EXPERIMENTAL MODEL AND SUBJECT DETAILS

**MICROBES—***Saccharomyces cerevisiae* strains (WT, *Δcoq9 and Δcoq7*) were the haploid MATalpha BY4742 (his3Δ1 leu2Δ0 lys2Δ0 ura3Δ0) from the gene deletion consortium (Thermo #YSC1054). *Escherichia coli* strains for protein overexpression were BL21[DE3]-RIPL and ArcticExpress (DE3) from Agilent (Cat#230280 and Cat#230192 respectively). *Escherichia coli* strain for DNA cloning and mutagenesis was DH5α from NEB (Cat#C2987). Please see individual methods for detailed culture conditions.

## METHOD DETAILS

**Site-directed mutagenesis and heat-shock transformation—**Yeast Coq7 and Coq9 point mutants were constructed as described in the Q5® Site-Directed Mutagenesis Kit (New England Biolabs) and were confirmed via Sanger sequencing. Plasmid p413 harboring wild

type Coq7 was used as a template. In the case of Coq9, pUC19 Coq9-FLAG plasmid was used as a template and successful mutants were cloned into p416 vector using EcoRI and BamHI restriction enzymes and T4 ligase (New England Biolabs). Yeast were transformed as previously described (Gietz and Woods, 2002). Briefly, single yeast colony was used to inoculate 5 mL of liquid culture (YEPD or selection media) and grown overnight at 30°C with shaking. Next, 1.5 mL of the culture was transferred to 50 mL of pre-warmed (30°C) TRAFO media and grown for 4h. Cells were pelleted by centrifugation 3000 g for 5 min. and washed twice with 50 mL of sterile water, resuspended in 1 mL of water, transferred to a 1.5 mL Eppendorf tube, and pelleted again. Next, the cells were resuspended in 1 mL of water, aliquoted (100 μL, ~1e8 cells) to individual tubes, pelleted again, and resuspended in ice-cold transformation mix (240 μL PEG 3500 50% w/v, 36 μL 1.0M Lithium Acetate, 50 μL boiled ssDNA, 34 μL of water with ~500 ng of plasmid DNA). Samples were vortexed vigorously to resuspend the cells and heat-shocked at 42°C for 40 min. in a water bath. Next, yeast were pelleted by 1 min. centrifugation at 10 000g, washed with 1.5 mL of water, spun at 3000g for 1 min., resuspended in 300 μL of water and plated onto S.C. selection media with 2% agar.

To generate pET24a hi6-GB1-Nd38_COQ7 the insert was amplified from pET30 GB1-Nd38_COQ7 with forward primer harboring NdeI cut site and his6 tag and reverse primer harboring EcoRI site. The amplicon and empty pET24a vector were cut with restriction enzymes, ligated with T4 ligase, and confirmed with Sanger sequencing. Bacteria were transformed with standard 30 sec. 42°C heat-shock method and plated on LB 2% agar media with selection.

**COQ7 purification—***E.coli* ArcticExpress cells harboring pET24a his6-GB1-Nd38_COQ7 (WT or mutants) were grown O/N at 37°C in 25 mL LB media supplemented with geneticin and kanamycin. Cells were refreshed in 3× 2L LB to $OD_{600}$=0.1 and grew with shaking at 37°C to $OD_{600}$=0.4. Cultures were chilled to 20°C, 100uM ammonium iron sulfate was added, and protein expression was induced with 100 μM Isopropyl β- d-1-thiogalactopyranoside (IPTG). After the first and the second hour 100 μM ammonium iron sulfate was added again. Protein production was continued for 24h total and then cells were spun 10 min. × 5000g at 4°C. Each 15g of cell paste were resuspended in 35 mL total Lysis Buffer (20 mM HEPES pH 7.5, 200 mM NaCl, 10% glycerol, 5 mM sodium thioglycolate, 1 mM cysteine, 1 μL Benzonase, 5 mM $MgCl_2$, 500 μM phenylmethylsulfonyl fluoride (PMSF), 0.1 mg/mL lysozyme) and incubated at 4°C with slow rotation. Next, the conical tubes were put on ice and the cells were lysed using Bronson sonifier (50% amplitude, 10 sec. ON/60 sec. OFF, 3 cycles). The lysate was spun (10 min. × 50 000g), supernatant was collected and the soluble fraction of COQ7 was subjected to IMAC purification on TALON resin as described later. The pelleted fraction containing membrane-bound COQ7 was resuspended in 10 mL of Lysis Buffer supplemented with 3% digitonin. Sample was loaded into syringe and further homogenized by passing it several times through a needle. The homogenate was incubated at 4°C with rotation for next 2h. Then, it was transferred to oakridge tube and Lysis Buffer was added to 30 mL total. Sample was spun 1h × 50 000g and supernatant containing solubilized proteins was loaded onto 5 mL of TALON resin equilibrated with Wash Buffer (20 mM HEPES 7.5, 200 mM NaCl, 10% glycerol,

1 mM imidazole) in 50 mL conical tube. After 2h incubation at 4°C with gentle rotation, the resin was washed 3 times with 50 mL of Wash Buffer + 10 mM imidazole. Next, the resin was transferred to 15 mL conical tube and the COQ7 was eluted with 5 mL of Elution Buffer (20 mM HEPES 7.5, 200 mM NaCl, 10% glycerol, 150 mM imidazole). Sample was incubated in ice for 10 min., spun 5 min. × 700g, supernatant was collected, and the resin was subjected to another round of elution. Supernatants were combined, concentrated to 1 mL using Amicon Centrifugal Filter (15k Da cut-off) and subjected to Size Exclusion Chromatography. Best fractions were pooled together, frozen with liquid nitrogen and stored at −80C.

**COQ9 and COQ7:COQ9 complex purification—***E.coli* Arctic Express cells harboring pETduet his6-Nd79_COQ9 alone or co-transformed with pET30 GB1-Nd38_COQ7 were grown O/N at 37°C in 25 mL LB media supplemented with geneticin, ampicillin and kanamycin as needed. Cells were refreshed in 3× 2L LB to $OD_{600}$=0.1 and grew with shaking at 37°C to $OD_{600}$=0.4. Cultures were chilled to 20°C, 100 μM ammonium iron sulfate was added, and protein expression was induced with 100 μM Isopropyl β- d-1-thiogalactopyranoside (IPTG). After the first and the second hour 100 μM ammonium iron sulfate was added again. Protein production was continued for 24h total and then cells were spun 10 min. × 5000g at 4°C. Each 15g of cell paste was resuspended in 35 mL total Lysis Buffer (20 mM HEPES pH 7.5, 200 mM NaCl, 10% glycerol, 5 mM sodium thioglycolate, 1 mM cysteine, 1 μL Benzonase, 5 mM $MgCl_2$, 500 μM phenylmethylsulfonyl fluoride (PMSF), 0.1 mg/mL lysozyme) and incubated at 4°C with slow rotation. Next, the conical tubes were put on ice and the cells were lysed using Bronson sonifier (50% amplitude, 10 sec. ON/60 sec. OFF, 3 cycles). The lysate was spun (30 min. × 50 000g) and the supernatant was loaded onto 5 mL of TALON resin equilibrated with Wash Buffer (20 mM HEPES 7.5, 200 mM NaCl, 10% glycerol, 1 mM imidazole) in 50 mL conical tube. After 2h incubation at 4°C with gentle rotation, the resin was washed 3 times with 50 mL of Wash Buffer + 10 mM imidazole. Next, the resin was transferred to 15 mL conical tube and proteins were eluted with 5 mL of Elution Buffer (20 mM HEPES 7.5, 200mM NaCl, 10% glycerol, 150 mM imidazole). Sample was incubated in ice for 10 min., spun 5 min. × 700g, supernatant was collected, and the resin was subjected to another round of elution. Supernatants were combined, concentrated to 1 mL using Amicon Centrifugal Filter (15k Da cut-off) and subjected to Size Exclusion Chromatography and subsequent blue native PAGE analysis (NativePAGE, 4–16%, Bis-Tris, Invitrogen).

**Size Exclusion Chromatography—**Purified proteins concentrated to 1 mL or gel filtration standards (BioRad, 1511901) were injected on to Hi-Load pg200 column and 150 mL eluate was collected as 1.0 mL fractions at 1.0 mL/min., in 20 mM HEPES pH 7.5, 200 mM NaCl buffer or in 20 mM ammonium acetate pH 7.0 in case of the COQ7:COQ9 complex subjected later to the cryo-EM. UV absorbance signal was used to detect protein-containing fractions which were then analyzed by SDS-PAGE (NuPAGE™ 4 to 12%, Bis-Tris, Invitrogen) to assess their purity. Best fractions were pooled together, frozen with liquid nitrogen and stored at −80°C.

**Lipids extraction from yeast—**Yeast were transformed with p413 or p416 plasmids carrying wild type or mutated version of yeast COQ7 and COQ9 genes, respectively. Next, individual colony was picked from the S.C. 2% glucose pABA- plate and used to start 3 mL liquid culture in the same media. After 12h growth at 30°C with shaking, the cultures were used to prepare new 3 mL cultures in S.C. 0.1% glucose, 3.0% glycerol, 50 nM pABA at $OD_{600}$=0.1 and incubated at 30C with shaking for 24h to pass the diauxic shift. Next, equivalent of 5 mL $OD_{600}$=1.0 (~5e7 cells) was pelleted (2 min. × 3000g) in 1.5 mL screw-cap tube. The supernatant was discarded, 100 μL of glass beads, and 50 μL of 150 mM KCl, and 600 μL of methanol with 0.1 μM $CoQ_8$ internal standard (Avanti Polar Lipids) were added, and the cells were lysed by 2 rounds of 5 min. bead-beating in disruptor genie set to max (3000 rpm) speed. To extract lipids, 400 μL of petroleum ether was added to sample and subjected to bead-beating for 3 min. Sample was then spun 2 min. × 1000g at 4°C and the ether layer (top) was transferred to a new tube. Extraction was repeated, the ether layers were combined and dried (~30 min.) under argon gas at room temperature.

**CoQ6 measurement by HPLC-ECD—**Extracted dried lipids were resuspended in 50 μL of mobile phase (78% methanol. 20% isopropanol, 2% 1 M ammonium acetate pH 4.4 in water and transferred to amber glass vials with inserts. Vials were inserted into HPLC (Ultimate 3000, Thermo Scientific) with electrochemical detector (ECD-3000RS) and 10 μL of each sample was injected. The flow rate was set to 0.3 mL/min (LPG-3400RS pump). The first electrode (6020RS) was set to +600 mV and placed before the column (Thermo Scientific, Betasil C18, 100 × 2.1 mm, 3um particle) to oxidize all the quinones and ensure their simultaneous elution. Second electrode (6011RS) was set to −600 mV to reduce the quinones exiting the column, and then the third electrode was set to +600 mV to make final recordings. A $CoQ_6$ standard (Avanti Polar Lipids) was used to identify corresponding peak in the obtained data. Peaks were then quantified with Chromeleon 7.2.10 software using cobra wizard option.

**Measurement of $DMQ_0$'s redox state by HPLC-ECD—**Samples were prepared according to "NADH fluorescence method". Briefly, reactions containing 500 μM NADH, 250 μM $DMQ_0$, and 5 μM protein when indicated were incubated for 0–5 minutes and quenched with 100 μL of −20°C cold methanol, incubated at −20°C for 5 min. and spun at 2°C for 5 min. × 20 000 g. Supernatants were layered with argon gas and transferred to amber glass vials. Vials were inserted into HPLC (Ultimate 3000, Thermo Scientific) with electrochemical detector (ECD-3000RS) and cooled to 4°C. Then, 2.5 μL of each sample was injected and resolved at 0.25 mL/min. (LPG-3400RS pump) isocratic flow of 90% A (0.1% formic acid in $H_2O$) and 10% B (isopropanol) mobile phase. The first electrode (6020RS) placed before the column (BetaBasic C18, 100 × 4.5 mm, 5um particle) was turned off (0 mV). Second electrode (6011RS) was set to −600 mV to reduce the quinones exiting the column, and then the third electrode was set to +600 mV to make final recordings. Data were compared to 250 μM $DMQ_0$ standard (aaBlocks) pre-oxidized with first electrode set to +600 mV or pre-reduced with the electrode set to −600 mV. All reactions were done in triplicate. Representative traces are shown. Additionally, areas of the peaks were quantified using Chromeleon software and used to calculate ratio of reduced $DMQ_0$ to oxidized $DMQ_0$.

**Western Blotting—**Methanol-glass beads mix from the lipid extraction protocol was dried under fume hood at 60°C for several hours until complete dryness. Next, 200 µL of 1x LDS Buffer with 10 mM DTT was added and the sample was boiled for 20 min. with often intense vortexing. Beads were spun 5 min. × 20 000g and 15 µL of supernatant was loaded on SDS-PAGE gel (NuPAGE™ 4 to 12%, Bis-Tris, Invitrogen). Proteins were electrophoretically separated for 35 min. at 150V, and then transferred (192 mM glycine, 25 mM Tris, 20% methanol [v/v]) to methanol-activated PVDF membrane (Immobilon-FL). The membrane was washed with TBS-T (20 mM Tris pH 7.4, 150 mM NaCl, 0.05% Tween 20 [v/v]), blocked with 5% powdered milk in TBS-T, washed 3 times with TBS-T, incubated at 4°C O/N with primary α-FLAG (Millipore F1804–5MG) or α-beta-Actin (Abcam ab8224) or α-Coq7 (raised by GenScript in rabbits against NLERTDGTKGPSEE peptide) antibodies (1:5000 in 0.5% milk), washed 3 times with TBS-T, incubated with secondary antibodies (1:20 000 in 0.1% milk, goat anti-mouse (LI-COR 926–32210, 1:15000; RRID: AB_621842) or goat anti-rabbit (LI-COR 926–32211, 1:15000; RRID: AB_621843)), washed 3 times with TBS-T, and finally visualized with LI-COR Odyessey CLx scanner using Image Studio v5.2 software.

**Yeast respiratory growth—**Individual colony was picked from the S.C. -URA or -HIS, 2% glucose, pABA-, plate and used to start 3 mL liquid culture in the same media. After 12h growth at 30°C with shaking, the culture was used to prepare new 1.0 mL culture in S.C. 0.1% glucose, 3.0% glycerol, 50 nM pABA at $OD_{600}$=0.05. Next, 100 µL of it was transferred to 96-well round-bottom clear plate (Thermo) and sealed with BreatheEasy film (USA Scientific). The plate was loaded into EPOCH plate reader operated with Gen5 3.1 software and yeast were grown at 30°C with max linear shaking (1096 cpm) for 48–72h with optical density monitored every 20 min. at 600 nm.

**COQ7:COQ9 complex delipidation—**100 µL of COQ9:COQ7 complex was thawed (20mM HEPES pH 7.5 200mM NaCl, 10% glycerol at 1.5 µg/µL) and incubated 1h with 100 µL BioBeads (washed with 1mL of methanol and then 3× 1mL buffer) at room temp with orbital shaking. In parallel, 100 µL of COQ9:COQ7 was incubated without biobeads as a control of protein stability at the room temp. 5 µL was collected after 1h. The beads were spun 15 000g × 1 min. and the supernatant containing delipidated complex was transferred to a new tube. The beads were washed 3 times with 1 mL of the buffer and resuspended in 100 µL of 1x LDS buffer with 5 mM DTT. Finally, blue native PAGE (NativePAGE, 4–16%, Bis-Tris, Invitrogen) and SDS-PAGE (NuPAGE™ 4 to 12%, Bis-Tris, Invitrogen) were run to analyze results.

**NADH fluorescence—**Buffer (20 mM HEPES pH 7.6, 200 mM NaCl) was mixed with 5 µM protein, 250 µM NADH, and 250 µM $DMQ_0$ as indicated in the figure to total reaction volume of 100 µL. Samples were loaded into black flat clear bottom 96-well plate (BRANDplates, pure-grade) and incubated at 30°C with constant slow orbital shaking. Optics were set to TOP position with probe's height at 5 mm and gain value 100. Then, NADH's fluorescence was recorded every 5 min. (Excitation= 340 nm, Emission=445 nm) for 4h.

**Differential Fluorimetry Scanning (DSF)—**24.5 μL of 5 μM solution of every protein was prepared in 96-well plate MicroAmp Optical plate (Applied biosystems), and incubated at room temp. for 15 min. Then, 0.5 μL 50x SYPRO Orange (Invitrogen) dye in 10% DMSO was added to each well and mixed by pipetting. The plate was sealed with MicroAmp Optical film (Applied biosystems), spun 1 min. × 1000 g, loaded into QuantStudio 6 Flex (Applied biosystems) and subjected to 20–99°C heat gradient changing at 0.025 °C/sec. Signal for ROX dye (overlapping with SYPRO orange) was recorded. The data were analyzed using DSFworld server (https://gestwickilab.shinyapps.io/dsfworld). Fits 2 and 4 were selected as the best representing the shape of melting curves and used to calculate melting temperatures.

***In silico* analyses—**Tunnels in COQ7 were detected with MOLEonline (Pravda et al., 2018) server (https://mole.upol.cz/) using default settings. All graphs were prepared using GraphPad Prism 9.1.0 software. All structures were analyzed (inter-residue distances, interactions etc.) and visualized using CHIMERA 1.11.2 software(Pettersen et al., 2004). Electrostatic surface potentials of proteins were calculated using APBS server (Jurrus et al., 2018) (poissonboltzmann.org) on default settings. Densitometry was performed with ImageJ 1.50i (Schneider et al., 2012). Student t-tests were calculated in Excel.

**Mass-spec lipidomics analysis of $DMQ_6$ content in yeast.—**Lipid extracts from equivalents of 5 mL $OD_{600}$=1.0 (~5e7 cells) yeast cultures were prepared as described in "HPLC-ECD" section. LC-MS analysis was performed using Thermo Vanquish Horizon UHPLC system coupled to a Thermo Exploris 240 Orbitrap mass spectrometer. For LC separation, A Vanquish binary pump system (Thermo Scientific) was used with a Waters Acquity CSH C18 column (100 mm × 2.1 mm, 1.7 mm particle size) held at 35°C under 300 μL/min flow rate. Mobile phase A consisted of 5 mM ammonium acetate in ACN/$H_2O$ (70:30, v/v) containing 125 μL/L acetic acid. Mobile phase B consisted of 5 mM ammonium acetate in IPA/ACN (90:10, v/v) with the same additive. For each sample run, mobile phase B was initially held at 2% for 2 min and then increased to 30% over 3 min. Mobile phase B was further increased to 50% over 1 min and 85% over 14 min and then raised to 99% over 1 min and held for 4 min. The column was re-equilibrated for 5 min at 2%B before the next injection. Five microliters of sample were injected by a Vanquish Split Sampler HT autosampler (Thermo Scientific) while the autosampler temperature was kept at 4 °C. The samples were ionized by a heated ESI source kept at a vaporizer temperature of 350°C. Sheath gas was set to 50 units, auxiliary gas to 8 units, sweep gas to 1 unit, and the spray voltage was set to 3,500 V for positive mode and 2,500 V for negative mode (two separate injections per replicate). The inlet ion transfer tube temperature was kept at 325°C with 70% RF lens. For discovery analysis, $MS^1$ scans were acquired at 120,000 resolution from m/z 200 to 1,700 with EasyIC enabled to improve mass accuracy. $MS^2$ scans were acquired in AcquireX Background Exclusion mode to automatically exclude background ions found in the extraction blank from MS/MS fragmentation during sample acquisitions with the cycle time of 1.5 s. Other $MS^2$ parameters include resolution of 30,000, 54 ms $MS^2$ ion injection time, 1.5 m/z isolation width, stepped HCD collision energy (25%, 30% for positive mode and 20%, 40%, 60% for negative mode), and 3 s dynamic exclusion. Automatic gain control (AGC) targets were set to standard mode for both $MS^1$ and $MS^2$ acquisitions.

**Data Analysis—**The resulting CoQ intermediate (oxidized form) data were processed using TraceFinder 5.1 (Thermo Fisher Scientific).

**LC-MS lipidomics of purified proteins and *E. coli* cells.—**For lipidomics analysis of COQ7:COQ9 complex, two 20 uL aliquots of 5 mg/mL protein COQ9:COQ7 complex, in 200 mM ammonium Acetate were extracted using Matyash method (Matyash et al., 2008). Briefly, once samples were thawed on ice, 200 μL methyl tert-butyl ether (MTBE), 60 uL of methanol, and 50 uL of water was added to each tube and the mixture was vortexed for 10 s. The sample was then centrifuged for 10 min at 10,000 g at 4°C. 150 μL of the lipophilic (upper) layer from the biphasic extraction was aliquoted into a separate glass vial and dried down by vacuum centrifugation, and was then resuspended in 50 μL 9:1 MeOH/Toluene prior to LC-MS/MS analysis.

For lipidomics of the separately purified proteins, two aliquots of each purified protein (100 μg COQ7, 100 μg COQ9, 200 μg COQ7:COQ9) or pelleted *E.coli* cells (10e10, ~20 × $OD_{600}$=1.0) were thawed on ice. Once thawed, 87 μL of methanol, and 290 μL methyl tert-butyl ether (MTBE) were added to each non-pellet tube and the mixture was vortexed for 10 s (sample contained 100 μL of aqueous buffer). For each of the *E. coli* cell pellet tubes, 205 μL methanol, 750 μL MTBE, and 187.5 μL water were added, and the mixture was sonicated for 10 s. After centrifugation for 2 min at 14,000 g at 4°C, 200 μL of the lipophilic (upper) layer from the biphasic extraction was aliquoted into an amber glass autosampler vial with glass insert and dried down by vacuum centrifugation. The samples were then resuspended in 50 μL 9:1 MeOH/toluene prior to LC-MS/MS analysis.

**LC-MS/MS analysis for lipidomics.—**Sample analysis was performed using an Acquity CSH C18 column held at 50 °C (100 mm × 2.1 mm × 1.7 μm particle size; Waters), a 400 μL/min flow rate was maintained using a Vanquish Binary Pump (Thermo Scientific). The mobile phases consisted of 10 mM ammonium acetate in ACN:H2O (70:30, v/v) with 250 μL/L acetic acid (Mobile Phase A), and 10 mM ammonium acetate in IPA:ACN (90:10, v/v) with 250 μL/L acetic acid (Mobile Phase B). For each sample 10 μL, was injected onto column using Vanquish autosampler (Thermo Scientific). The gradient for lipid separations was as follows, mobile phase B was initially held at 2% for 2 min and then increased to 30% over 3 min. Mobile phase B was further increased to 50% over 1 min, then raised to 85% over 14 min, and finally raised to 99% over 1 min and held at 99 % for 7 min. The column was re-equilibrated with mobile phase B at 2% for 1.75 min before the next injection.

The LC system was coupled to a Q Exactive Orbitrap mass spectrometer through a heated electrospray ionization (HESI II) source (Thermo Scientific). Source conditions were as follow: HESI II and capillary temperature at 300 °C, sheath gas flow rate at 25 units, aux gas flow rate at 15 units, sweep gas flow rate at 5 units, spray voltage at |3.5 kV| for both positive and negative modes, and S-lens RF at 90.0 units. Data were acquired using polarity switching with positive and negative full MS and MS2 spectra (Top2) within the same injection. Acquisition parameters for full MS scans in both modes were 17,500 resolution, $1 \times 10^6$ automatic gain control (AGC) target, 100 ms max inject time, and 200 to 1600 m/z scan range. MS2 scans in both modes were then performed at 17,500 resolution, $1 \times 10^5$

AGC target, 50 ms max IT, 1.0 m/z isolation window, stepped normalized collision energy (NCE) at 20, 30, 40, and a 10.0 s dynamic exclusion

**Data Analysis for lipidomics by mass spectrometry—**LC–MS data were processed using Compound Discoverer 2.1 and 3.1 (Thermo Scientific) and LipiDex, an in-house-developed software suite (Hutchins et al., 2018). Features detection was performed within a 1.4 min to 21 min retention time window, and features were aggregated into compound groups using a 10-ppm mass and 0.75 min retention time tolerance. Detect compounds node settings of minimum peak intensity of $5\times10^5$, maximum peak-width of 0.75, and signal-to-noise (S/N) ratio of 3 were used. Background features were designated as features less than 3-fold intensity over blanks and were excluded from further processing. MS/MS spectra were searched against an in-silico generated lipid spectral library (Hutchins et al., 2018). Spectral matches with a dot product score greater than 500 and a reverse dot product score greater than 700, eluting within a 3.5 median absolute retention time deviation (M.A.D. RT) of each other, and found within at least 2 processed files were retained. Lipids with no significant interference (<75 %) from co-eluting isobaric lipids were identified at the individual fatty acid substituent level, otherwise lipids were annotated with the sum of the fatty acid substituents.

**In-gel sample digestion for proteomics—**All the steps were performed at room temperature with use of LC-MS grade reagents. Samples were loaded onto reducing SDS-PAGE gel (NuPAGE™ 4 to 12%, Bis-Tris, Invitrogen) and resolved 45 min. × 150V. Individual bands were excised from the gel, placed in separate tubes and cut into smaller pieces. Samples were destined for 15 min. in 100 μL of 25 mM ammonium bicarbonate (AMBIC) in acetonitrile/water (50/50, v/v) buffer. Next, samples were washed for 10 min. with acetonitrile and air dried for 10 min. Then, samples were reduced (40 μL of 10 mM TCEP and 40 mM 2-chloroacetemide in 25 mM AMBIC) for 30 min. and dehydrated in 200 μL acetonitrile for 10 min. The gel pieces were air dried for 10 min., incubated with 40 μL of trypsin (Promega, Sequencing Grade, 16 ng/μL in 25 mM AMBIC) for 15 min., supplemented with additional 30 μL of 25 mM AMBIC and the proteins were digested overnight. Supernatants containing digested peptides were transferred to new tubes and gel pieces were covered with 100 μL extraction buffer (5% formic acid in water/acetonitrile (1/2, v/v), incubated for 10 min. and the supernatants were collected and combined with the previous ones. Samples were dried down to several μL in Speedvac (Thermo Scientific), resuspended in 100 uL 0.1% TFA and desalted using C18 Omix tips (Agilent, #A57003100K). Each time a tip was conditioned with 2× 100 μL of 0.1% TFA in 50:50 (v/v) ACN/$H_2O$, washed with 2× 100 μL of 0.1% TFA in $H_2O$, sample was bound by passing 10 times thru tip resin, and then washed 3× 100 μL of 0.1% TFA in $H_2O$. The peptides were eluted with 100 μL of 0.1% TFA in 80:20 (v/v) ACN/$H_2O$, dried in Speedvac, reconstituted in 20 μL of 0.2% formic acid in $H_2O$ and subjected to LC-MS analysis.

**Liquid Chromatography Mass Spectrometry Proteomics—**LC separation was performed using Thermo Ultimate 3000 RSLCnano system. A 15 cm EASY-Spray™ PepMap™ RSLC C18 column (150 mm × 75 μm, 3 μm) was used at 300 nL/min flow rate with a 60 min. gradient using mobile phase A consisting of 0.1% formic acid in $H_2O$,

and mobile phase B consisting of 0.1% formic acid in ACN/$H_2O$ (80/20, v/v). EASY-Spray source was used and temperature was at 35 °C. Each sample run was held at 4.0% B for 3 min and increased to 45% B over 42 min, followed by 5 min at 95% B and back to 4% B for equilibration for 10 min. An Acclaim PepMap C18 HPLC trap column (20 mm × 75 μm, 3 μm) was used for sample loading. MS detection was performed with Thermo Exploris 240 Orbitrap mass spectrometer in positive mode. The source voltage was set to 1.5 kV, ion transfer tube temperature was set to 275 °C, RF lens was at 40%. Full MS spectra were acquired from m/z 350 to 1400 at the Orbitrap resolution of 120000, with the normalized AGC target of 300% (3E6) and max ion injection time of 25 ms. Data-dependent acquisition (DDA) was performed for the top 15 precursor ions with the charge state of 2–6 and an isolated width of 2. Intensity threshold was 5E3. Dynamic exclusion was 20 s with the exclusion of isotopes. Other settings for DDA include Orbitrap resolution of 15000, HCD collision energy of 30%, and ion injection time of 40 ms.

Raw data files were analyzed by Andromeda Search engine incorporated in MaxQuant v1.6.17.0 software against human and *E. Coli* databases downloaded from Uniprot. Label-free quantitation was enabled in the analysis to compute iBAQ values for the identified proteins.

**Negative-stain electron microscopy—**4.0 μl aliquots of purified COQ7-COQ9 complex (0.05 mg $ml^{-1}$) was applied onto glow-discharged continuous carbon-coated grids, blotted with filter paper, and stained with freshly prepared 0.75% (w/v) uranyl formate. Negatively-stained electron microscopy grids were imaged on Tecnai T12 microscope (FEI Company) equipped with a 4k × 4k CCD camera (UltraScan 4000, Gatan) and operated at a voltage of 120 kV. Images were recorded at room temperature with a nominal magnification of 52,000x, corresponding to a calibrated pixel size of 2.21 Å on the specimen. A total of 121 micrographs were collected and CTF parameters were estimated by CTFFIND4 (Rohou and Grigorieff, 2015). Particles were manually picked, extracted with a box size of 200 × 200 pixels, and reference-free 2D classification was used to generate the templated for the automatic particle picking by using Relion 3.0 software package (Zivanov et al., 2018). Then, 262,589 particle projections were semi-automatically picked from the micrographs and sorted through multiple rounds of 2D classification to discard poorly defined particle classes using Relion 3.0. A subset of 231,879 particles with well-defined shapes was selected following multiple rounds of 2D classification to demonstrate 2D class averages of COQ7-COQ9 complex.

**Cryo-EM sample preparation—**Peak fractions containing the COQ7-COQ9 complex were concentrated to 5 mg $ml^{-1}$ and flash frozen in liquid nitrogen for long-term storage at −80 °C. An aliquot of purified COQ7-COQ9 complex was diluted to 0.5 mg $ml^{-1}$ (8.8 μM) in 200mM Ammonium Acetate, pH 7.0 before blotting. Cryo-EM samples of COQ7-COQ9 complex bound to NADH were prepared similarly with the addition of NADH. Briefly, the diluted complex (8.8 μM) was mixed with NADH to a final NADH concentration of 5 mM in a final solution containing 200mM Ammonium Acetate, pH 7.0, and incubated at room temperature for 1 hour. To prepare cryo-EM grids, 3.5 μl of purified COQ7-COQ9 complex was applied to glow-discharged holey carbon grids (Quantifoil R1.2/1.3, 400 mesh Cu) and

incubated for an additional 30 s. Then, the grids were blotted with Whatman Grade 1 filter paper (Whatman) for ~6 s with a 0 mm offset at 10 °C and 100% relative humidity and plunge frozen into liquid ethane using a Vitrobot Mark IV (Thermo Fisher Scientific).

**Data collection—**Two datasets were collected on two different microscopes using the multi-record strategy (nine-hole exposures per single-stage movement) in SerialEM software (Mastronarde, 2005). For unliganded COQ7-COQ9 complex, images were collected on a FEI Talos Arctica equipped with a K3 Summit direct electron detector (Gatan) and operated at an accelerating voltage of 200 keV. In total, 1,395 images were recorded with a defocus range of −0.5 to −1.5 μm in super-resolution counting mode at a nominal magnification of 36,000x, corresponding to a super-resolution pixel size of 0.57 Å (physical pixel size of 1.14 Å) on the specimen level. Each image was dose-fractionated over 120 frames with a per frame dose rate of ~0.49 electrons and total exposure time of 2.4 s, resulting in an accumulated dose of ~58.8 electrons per $Å^2$. For NADH-bound COQ7-COQ9 complex, images were acquired on a FEI Titan Krios equipped with a K3 Summit direct electron detector and a Quantum GIF energy filter (Gatan) with a slit width of 20 eV and operated an accelerating voltage of 300 keV in nano-probe mode. A total of 10,088 micrographs were collected at a magnification of 105,000x with a calibrated super-resolution pixel size of 0.4165 Å (physical pixel size of 0.833 Å) and a defocus range of −0.3 to −1.2 μm. The total exposure time for each micrograph was 3 s, with dose-fractionation set at 0.025 s per frame, resulting in 118 movie frames at a per frame dose rate of ~0.55 electrons for a total accumulated dose of ~65 electrons per $Å^2$. Data collection statistics are shown in Extended Data Table 1.

**Image analysis and 3D reconstruction—**Dose-fractionated stacks were subjected to beam-induced motion correction using MotionCor2 (Zheng et al., 2017). CTF parameters for each micrograph in the unliganded COQ7-COQ9 complex and the NADH-bound COQ7-COQ9 complex datasets were determined by GCTF v.1.06 (Zhang, 2016) and CTFFIND4 (Rohou and Grigorieff, 2015), respectively. Subsequent image processing for both datasets was carried out in Relion 3.0. For cofactor-free COQ7-COQ9 complex, 3040 particles were manually picked and classified by reference-free 2D classification to generate templates for automatic particle picking. A total of 574,760 auto-picked particles were extracted with a box size of 192 pixels and subjected to two rounds of 2D classification to discard poorly defined classes, resulting in 528,971 particles for further processing. An initial 3D model from these particles was generated by using cryoSPARC *ab initio* reconstruction(Punjani et al., 2017). Stable classes were then used for iterative rounds of 3D refinement and reclassification without symmetry. Upon visual inspection of 3D reconstructions in UCSF Chimera(Pettersen et al., 2004), the particles from the best 3D classes (281,866 particles) were combined and subjected to 3D refinement with D2 symmetry. Subsequent per-particle CTF refinement and 3D classification without alignment yielded a single class containing 61,526 particles. This final subset of particles was refined with a soft mask and sharpened by a negative temperature factor to a resolution of 3.5 Å during post-processing procedure. A similar strategy was used for NADH-bound COQ7-COQ9 complex. In total, 2,709,398 particles were extracted with a box size of 256 pixels and binned to 128 pixels. After removing the suboptimal particles with two rounds of reference-free 2D classification, the

best classes were subjected to 3D refinement without imposed symmetry. Subsequent 3D classification into 6 classes showed two dominant classes containing 1,249,119 particles (~46% of the dataset), which was then re-extracted to a box size of 256 pixels and refined with D2 symmetry imposed. These particles were subjected to another round of 3D classification into six classes without image alignment, resulting in 372,917 particles with indicated global resolution of 2.7 Å. The map was further improved after CTF and aberration refinements by using Relion 3.1 (Zivanov et al., 2018). The final map had a resolution of 2.4 Å after sharpened by applying a negative temperature factor during the post-processing step. The reported final resolution estimates are based on the gold-standard Fourier shell correlation (FSC) cut-off of 0.143. Local resolutions were determined using ResMap with half-reconstructions as input maps. Refinement parameters for the final density maps are listed in Extended Data Table 1.

**Model building and validation—**The initial model of COQ7 was a homology model calculated by Phyre2(Kelley et al., 2015), using the intensive modeling mode. The crystal structure of COQ9 (PDB ID: 6AWL) was also used as an initial template for model building. The atomic models were manually rebuilt using Coot (Emsley et al., 2010) and real-space refined using *phenix.real_space_refine* tool (Afonine et al., 2018) from the PHENIX software package(Liebschner et al., 2019). Briefly, *phenix.mtriage*(Liebschner et al., 2019) was used to analyze cryo-EM maps and an automated sharpening procedure (*phenix.auto_sharpen* (Mastronarde, 2005)) was applied to the final cryo-EM reconstructions prior to model building. The 3.7 Å and 2.4 Å density maps were of sufficient quality for *de novo* model building. After initial model building, the unliganded and NADH-bound starting models were subjected to iterative rounds of refinement in *phenix.real_space_refine* using global minimization, morphing, noncrystallographic symmetry (NCS), B-factor refinement, local grid search and secondary structure restraints, and manual rebuilding in Coot. The ligand coordinates were docked into densities and refined using Coot. The final model geometry was evaluated using MolProbity 4.5(Williams et al., 2018). Independent FSC curves for model-map correlations were calculated between the resulting model and the half map used for refinement as well as between the resulting model and the other half map for cross-validation. Protein interfaces and associated free energies were analyzed by using PDBePISA server(Krissinel and Henrick, 2007). The final refinement statistics are summarized in Extended Data Table 1.

**Molecular dynamics simulations—**We prepared all systems for MD simulations with the membrane module of the CHARMM-GUI server(Lee et al., 2018) and followed the provided equilibration and production files, except for changes as indicated.

We parametrized the protein components with the CHARMM36m forcefield, its adapted TIP3P water model and the CHARMM36 lipids(Huang et al., 2017), and used the NADH parameters from (Pavelites et al., 1997) and the $CoQ_{10}$ parameters from (Teixeira and Arantes, 2019, Galassi and Arantes, 2015). For DMQ we utilized the parameters computed automatically by the CHARMM general force field (Vanommeslaeghe et al., 2010, Vanommeslaeghe and MacKerell, 2012) as implemented in CHARMM-GUI (Lee et al., 2018). The model membranes contained 17% cardiolipin (charged -2), 44% POPC and

39% POPE; or 16% cardiolipin, 42% POPC and 38% POPE when 4% CoQ10 was included (Kaurola et al., 2016). The solvent included 0.15 M KCl for charge neutralization and ionic strength.

For simulations aimed at testing unbinding of CoQ10 from COQ7's active site, we first tried replica exchange MD but it invariably resulted in membrane destabilization. Therefore, we took another approach in which we ran regular simulations at 300, 400, 450, 500 and 600 K. At 500 and 600 K, the system destabilized within the first few hundred nanoseconds of simulation times: the proteins unfolded and the membranes disrupted. At 300 and 400 K, the small molecule remained locked inside the active site for the full length of independent multi-microsecond trajectories. At 450 K we observed events in which the docked CoQ10 dissociated from the active site without compromising the protein or membrane stabilities within the simulated timescale (~1–1.5 microsecond); we therefore analyzed 10 independent replicas at this temperature as described in the main text. In all these simulations the membranes and proteins remained stable, and the NADH remained stably bound to COQ7, during the whole simulation times.

We ran all simulations with Gromacs 2020 (Abraham et al., 2015), visualized them with VMD(Humphrey et al., 1996) and analyzed them with custom scripts, VMD procedures, and the MEMBPLUGIN plugin for VMD (Guixà-González et al., 2014).

### QUANTIFICATION AND STATISTICAL ANALYSIS

See each individual method and figures' legends for the associated statistical analysis. The majority of p values in this report were calculated using an unpaired, one-sided, Student's t test. MS data analysis was performed as described in each MS analysis section. In all cases, *n* represents independent replicates of an experiment and error bars represent standard deviation. All Western Blots were done in triplicates and representative membranes are shown.

## Supplementary Material

Refer to Web version on PubMed Central for supplementary material.

## ACKNOWLEDGEMENTS

We thank current and former members of the D.J.P. and A.F. laboratories for helpful discussions and assistance, including Danielle C. Lohman for pioneering the purification of the COQ7:COQ9 complex, and Annie Jen and Zixiang Fang for help with mass-spectrometry. We also thank Professor Stephen J. Lippard for kindly providing the pET30 GB1-Nd38_COQ7 vector. M. Braunfeld, D. Bulkley, M. Harrington, A. Myasnikov, and Z. Yu of the UCSF Center for Advanced Cryo-EM for microscopy supportPaul Thomas, J. Baker-LePain and the QB3 shared cluster (NIH grants 1S10OD021596-01, S10OD020054, S10OD026881, 1S10OD021741 and the Howard Hughes Medical Institute).

This work was supported by NIH awards R35 GM131795 (D.J.P.), P41 GM108538 (J.J.C. and D.J.P.), support from the Howard Hughes Medical Institute Faculty Scholar program and the Chan Zuckerberg Biohub (A.F.); funds from the BJC Investigator Program (D.J.P.); and SNSF grants 205321_192371 and 31003A_170154 (M.D.P).

H.A. is a Human Frontier Science Program Long-Term Fellow supported by The International Human Frontier Science Program Organization (LT000398/2017-L).

## REFERENCES


ABRAHAM MJ, MURTOLA T, SCHULZ R, PÁLL S, SMITH JC, HESS B & LINDAHL E 2015. GROMACS: High performance molecular simulations through multi-level parallelism from laptops to supercomputers. SoftwareX, 1, 19–25.

ACOBA MG, SENOO N & CLAYPOOL SM 2020. Phospholipid ebb and flow makes mitochondria go. Journal of Cell Biology, 219, e202003131. [PubMed: 32614384]

AFONINE PV, POON BK, READ RJ, SOBOLEV OV, TERWILLIGER TC, URZHUMTSEV A & ADAMS PD 2018. Real-space refinement in PHENIX for cryo-EM and crystallography. Acta Crystallographica. Section D, Structural Biology, 74, 531–544. [PubMed: 29872004]

ALLAN CM, AWAD AM, JOHNSON JS, SHIRASAKI DI, WANG C, BLABY-HAAS CE, MERCHANT SS, LOO JA & CLARKE CF 2015. Identification of Coq11, a New Coenzyme Q Biosynthetic Protein in the CoQ-Synthome in Saccharomyces cerevisiae *. Journal of Biological Chemistry, 290, 7517–7534. [PubMed: 25631044]

ANDREWS SC 2010. The Ferritin-like superfamily: Evolution of the biological iron storeman from a rubrerythrin-like ancestor. Biochimica et Biophysica Acta (BBA) - General Subjects, 1800, 691–705. [PubMed: 20553812]

AUSILI A, TORRECILLAS A, ARANDA F, GODOS AD, SÁNCHEZ-BAUTISTA S, CORBALÁN-GARCÍA S & GÓMEZ-FERNÁNDEZ JC. 2008. Redox State of Coenzyme Q10 Determines Its Membrane Localization. The Journal of Physical Chemistry B, 112, 12696–12702. [PubMed: 18795772]

AUSSEL L, PIERREL F, LOISEAU L, LOMBARD M, FONTECAVE M & BARRAS F 2014. Biosynthesis and physiology of coenzyme Q in bacteria. Biochimica et Biophysica Acta (BBA) - Bioenergetics, 1837, 1004–1011. [PubMed: 24480387]

BEHAN RK & LIPPARD SJ 2010. The Aging-Associated Enzyme CLK-1 Is a Member of the Carboxylate-Bridged Diiron Family of Proteins. Biochemistry, 49, 9679–9681. [PubMed: 20923139]

BOLTON JL, TRUSH MA, PENNING TM, DRYHURST G & MONKS TJ 2000. Role of Quinones in Toxicology †. Chemical Research in Toxicology, 13, 135–160. [PubMed: 10725110]

BUDIN I, ROND TD, CHEN Y, CHAN LJG, PETZOLD CJ & KEASLING JD 2018. Viscous control of cellular respiration by membrane lipid composition. Science, 362, 1186–1189. [PubMed: 30361388]

CHEHADE MH, PELOSI L, FYFE CD, LOISEAU L, RASCALOU B, BRUGIÈRE S, KAZEMZADEH K, VO C-D-T, CICCONE L, AUSSEL L, COUTÉ Y, FONTECAVE M, BARRAS F, LOMBARD M & PIERREL F 2019. A Soluble Metabolon Synthesizes the Isoprenoid Lipid Ubiquinone. Cell Chemical Biology, 26, 482–492.e7. [PubMed: 30686758]

COX J & MANN M 2008. MaxQuant enables high peptide identification rates, individualized p.p.b.-range mass accuracies and proteome-wide protein quantification. Nat Biotechnol, 26, 1367–72. [PubMed: 19029910]

CRANE FL 2007. Discovery of ubiquinone (coenzyme Q) and an overview of function. Mitochondrion, 7, S2–S7. [PubMed: 17446142]

DANHAUSER K, HEREBIAN D, HAACK TB, RODENBURG RJ, STROM TM, MEITINGER T, KLEE D, MAYATEPEK E, PROKISCH H & DISTELMAIER F 2016. Fatal neonatal encephalopathy and lactic acidosis caused by a homozygous loss-of-function variant in COQ9. European Journal of Human Genetics, 24, 450–454. [PubMed: 26081641]

DUNCAN AJ, BITNER-GLINDZICZ M, MEUNIER B, COSTELLO H, HARGREAVES IP, LÓPEZ LC, HIRANO M, QUINZII CM, SADOWSKI MI, HARDY J, SINGLETON A, CLAYTON PT & RAHMAN S 2009. A Nonsense Mutation in COQ9 Causes Autosomal-Recessive Neonatal-Onset Primary Coenzyme Q10 Deficiency: A Potentially Treatable Form of Mitochondrial Disease. The American Journal of Human Genetics, 84, 558–566. [PubMed: 19375058]

EISENBERG-BORD M, TSUI HS, ANTUNES D, FERNÁNDEZ-DEL-RÍO L, BRADLEY MC, DUNN CD, NGUYEN TPT, RAPAPORT D, CLARKE CF & SCHULDINER M 2019. The Endoplasmic Reticulum-Mitochondria Encounter Structure Complex Coordinates Coenzyme Q Biosynthesis. Contact, 2, 2515256418825409. [PubMed: 30937424]

EMSLEY P, LOHKAMP B, SCOTT WG & COWTAN K 2010. Features and development of Coot. Acta Crystallographica Section D: Biological Crystallography, 66, 486–501. [PubMed: 20383002]

FATO R, BATTINO M, ESPOSTI MD, CASTELLI GP & LENAZ G 1986. Determination of partition and lateral diffusion coefficients of ubiquinones by fluorescence quenching of n-(9-anthroyloxy)stearic acids in phospholipid vesicles and mitochondrial membranes. Biochemistry, 25, 3378–3390. [PubMed: 3730366]

FERNÁNDEZ-DEL-RÍO L, KELLY ME, CONTRERAS J, BRADLEY MC, JAMES AM, MURPHY MP, PAYNE GS & CLARKE CF 2020. Genes and lipids that impact uptake and assimilation of exogenous coenzyme Q in Saccharomyces cerevisiae. Free Radical Biology and Medicine, 154, 105–118. [PubMed: 32387128]

FLOYD BRENDAN, J. WILKERSON, EMILY M, VELING MIKE, T. MINOGUE, CATIE E, XIA C, BEEBE EMILY, T. WROBEL, RUSSELL L, CHO H, KREMER LAURA, S. ALSTON, CHARLOTTE L, GROMEK KATARZYNA, A. DOLAN, BRENDAN K., ULBRICH A, STEFELY, JONATHAN A, BOHL SARAH, L. WERNER, KELLY M, JOCHEM A, WESTPHALL, MICHAEL S, RENSVOLD JARRED, W. TAYLOR, ROBERT W, PROKISCH H, KIM J-JAP, COON, JOSHUA J. & PAGLIARINI DAVIDJ. 2016. Mitochondrial Protein Interaction Mapping Identifies Regulators of Respiratory Chain Function. Molecular Cell, 63, 621–632. [PubMed: 27499296]

FORNERIS F & MATTEVI A 2008. Enzymes Without Borders: Mobilizing Substrates, Delivering Products. Science, 321, 213–216. [PubMed: 18621661]

FREYER C, STRANNEHEIM H, NAESS K, MOURIER A, FELSER A, MAFFEZZINI C, LESKO N, BRUHN H, ENGVALL M, WIBOM R, BARBARO M, HINZE Y, MAGNUSSON M, ANDEER R, ZETTERSTRÖM RH, DÖBELN UV, WREDENBERG A & WEDELL A 2015. Rescue of primary ubiquinone deficiency due to a novel COQ7 defect using 2,4–dihydroxybensoic acid. Journal of Medical Genetics, 52, 779. [PubMed: 26084283]

GALASSI VV & ARANTES GM 2015. Partition, orientation and mobility of ubiquinones in a lipid bilayer. Biochimica et Biophysica Acta (BBA) - Bioenergetics, 1847, 1560–1573. [PubMed: 26255075]

GARCÍA-CORZO L, LUNA-SÁNCHEZ M, DOERRIER C, GARCÍA JA, GUARÁS A, ACÍN-PÉREZ R, BULLEJOS-PEREGRÍN J, LÓPEZ A, ESCAMES G, ENRÍQUEZ JA, ACUÑA-CASTROVIEJO D & LÓPEZ LC 2013. Dysfunctional Coq9 protein causes predominant encephalomyopathy associated with CoQ deficiency. Human Molecular Genetics, 22, 1233–1248. [PubMed: 23255162]

GIETZ RD & WOODS RA 2002. Transformation of yeast by lithium acetate/single-stranded carrier DNA/polyethylene glycol method. Methods in Enzymology, 350, 87–96. [PubMed: 12073338]

GORBUNOVA V & SELUANOV A 2002. CLK-1 protein has DNA binding activity specific to OL region of mitochondrial DNA. FEBS Letters, 516, 279–284. [PubMed: 11959146]

GRAY HB & WINKLER JR 2003. Electron tunneling through proteins. Quarterly Reviews of Biophysics, 36, 341–372. [PubMed: 15029828]

GRAY HB & WINKLER JR 2005. Long-range electron transfer. Proc Natl Acad Sci U S A, 102, 3534–9. [PubMed: 15738403]

GUIXÀ-GONZÁLEZ R, RODRIGUEZ-ESPIGARES I, RAMÍREZ-ANGUITA JM, CARRIÓ-GASPAR P, MARTINEZ-SEARA H, GIORGINO T & SELENT J 2014. MEMBPLUGIN: studying membrane complexity in VMD. Bioinformatics, 30, 1478–1480. [PubMed: 24451625]

GUO X, NIEMI NM, COON JJ & PAGLIARINI DJ 2017. Integrative proteomics and biochemical analyses define Ptc6p as the Saccharomyces cerevisiae pyruvate dehydrogenase phosphatase. Journal of Biological Chemistry, 292, 11751–11759. [PubMed: 28539364]

HAMMES-SCHIFFER S & STUCHEBRUKHOV AA 2010. Theory of coupled electron and proton transfer reactions. Chem Rev, 110, 6939–60. [PubMed: 21049940]

HAUß T, DANTE S, HAINES TH & DENCHER NA 2005. Localization of coenzyme Q10 in the center of a deuterated lipid membrane by neutron diffraction. Biochimica et Biophysica Acta (BBA) - Bioenergetics, 1710, 57–62. [PubMed: 16199002]

HE CH, XIE LX, ALLAN CM, TRAN UC & CLARKE CF 2014. Coenzyme Q supplementation or over-expression of the yeast Coq8 putative kinase stabilizes multi-subunit Coq polypeptide

complexes in yeast coq null mutants. Biochimica et Biophysica Acta (BBA) - Molecular and Cell Biology of Lipids, 1841, 630–644. [PubMed: 24406904]

HIDALGO-GUTIÉRREZ A, GONZÁLEZ-GARCÍA P, DÍAZ-CASADO ME, BARRIOCANAL-CASADO E, LÓPEZ-HERRADOR S, QUINZII CM & LÓPEZ LC 2021. Metabolic Targets of Coenzyme Q10 in Mitochondria. Antioxidants, 10, 520. [PubMed: 33810539]

HSIEH EJ, GIN P, GULMEZIAN M, TRAN UC, SAIKI R, MARBOIS BN & CLARKE CF 2007. Saccharomyces cerevisiae Coq9 polypeptide is a subunit of the mitochondrial coenzyme Q biosynthetic complex. Archives of Biochemistry and Biophysics, 463, 19–26. [PubMed: 17391640]

HSU AY, DO TQ, LEE PT & CLARKE CF 2000. Genetic evidence for a multi-subunit complex in the O-methyltransferase steps of coenzyme Q biosynthesis. Biochimica et Biophysica Acta (BBA) - Molecular and Cell Biology of Lipids, 1484, 287–297. [PubMed: 10760477]

HUANG J, RAUSCHER S, NAWROCKI G, RAN T, FEIG M, GROOT BLD, GRUBMÜLLER H & MACKERELL AD 2017. CHARMM36m: an improved force field for folded and intrinsically disordered proteins. Nature Methods, 14, 71–73. [PubMed: 27819658]

HUMPHREY W, DALKE A & SCHULTEN K 1996. VMD: Visual molecular dynamics. Journal of Molecular Graphics, 14, 33–38. [PubMed: 8744570]

HUNG V, ZOU P, RHEE H-W, UDESHI NAMRATA, D. CRACAN, V. SVINKINA, T. CARR, STEVEN A, MOOTHA, VAMSI K. & ALICE Y TING. 2014. Proteomic Mapping of the Human Mitochondrial Intermembrane Space in Live Cells via Ratiometric APEX Tagging. Molecular Cell, 55, 332–341. [PubMed: 25002142]

HUTCHINS PD, RUSSELL JD & COON JJ 2018. LipiDex: An Integrated Software Package for High-Confidence Lipid Identification. Cell Syst, 6, 621–625 e5. [PubMed: 29705063]

HUTH JR, BEWLEY CA, CLORE GM, GRONENBORN AM, JACKSON BM & HINNEBUSCH AG 1997. Design of an expression system for detecting folded protein domains and mapping macromolecular interactions by NMR. Protein Science, 6, 2359–2364. [PubMed: 9385638]

JASNIEWSKI AJ & QUE L 2018. Dioxygen Activation by Nonheme Diiron Enzymes: Diverse Dioxygen Adducts, High-Valent Intermediates, and Related Model Complexes. Chemical Reviews, 118, 2554–2592. [PubMed: 29400961]

JONASSEN T, PROFT M, RANDEZ-GIL F, SCHULTZ JR, MARBOIS BN, ENTIAN K-D & CLARKE CF 1998. Yeast Clk-1 Homologue (Coq7/Cat5) Is a Mitochondrial Protein in Coenzyme Q Synthesis*. Journal of Biological Chemistry, 273, 3351–3357. [PubMed: 9452453]

JURRUS E, ENGEL D, STAR K, MONSON K, BRANDI J, FELBERG LE, BROOKES DH, WILSON L, CHEN J, LILES K, CHUN M, LI P, GOHARA DW, DOLINSKY T, KONECNY R, KOES DR, NIELSEN JE, HEAD-GORDON T, GENG W, KRASNY R, WEI GW, HOLST MJ, MCCAMMON JA & BAKER NA 2018. Improvements to the APBS biomolecular solvation software suite. Protein Science, 27, 112–128. [PubMed: 28836357]

KATSIKAS H & QUINN PJ 1983. Fluorescence Probe Studies of the Distribution of Ubiquinone Homologues in Bilayers of Dipalmitoylglycerophosphocholine. European Journal of Biochemistry, 131, 607–612. [PubMed: 6687712]

KAUROLA P, SHARMA V, VONK A, VATTULAINEN I & RÓG T 2016. Distribution and dynamics of quinones in the lipid bilayer mimicking the inner membrane of mitochondria. Biochimica et Biophysica Acta (BBA) - Biomembranes, 1858, 2116–2122. [PubMed: 27342376]

KELLEY LA, MEZULIS S, YATES CM, WASS MN & STERNBERG MJE 2015. The Phyre2 web portal for protein modeling, prediction and analysis. Nature Protocols, 10, 845–858. [PubMed: 25950237]

KEMMERER ZA, ROBINSON KP, SCHMITZ JM, MANICKI M, PAULSON BR, JOCHEM A, HUTCHINS PD, COON JJ & PAGLIARINI DJ 2021. UbiB proteins regulate cellular CoQ distribution in Saccharomyces cerevisiae. Nature Communications, 12, 4769.

KIRBY CS & PATEL MR 2021. Elevated mitochondrial DNA copy number found in ubiquinone-deficient clk-1 mutants is not rescued by ubiquinone precursor 2–4-dihydroxybenzoate. Mitochondrion, 58, 38–48. [PubMed: 33581333]

KRISSINEL E & HENRICK K 2007. Inference of Macromolecular Assemblies from Crystalline State. Journal of Molecular Biology, 372, 774–797. [PubMed: 17681537]

KUCUKELBIR A, SIGWORTH FJ & TAGARE HD 2014. Quantifying the local resolution of cryo-EM density maps. Nat Methods, 11, 63–5. [PubMed: 24213166]

KWONG AKY, CHIU ATG, TSANG MHY, LUN KS, RODENBURG RJT, SMEITINK J, CHUNG BHY & FUNG CW 2019. A fatal case of COQ7-associated primary coenzyme Q10 deficiency. JIMD Reports, 47, 23–29. [PubMed: 31240163]

LEE J, PATEL DS, STÅHLE J, PARK S-J, KERN NR, KIM S, LEE J, CHENG X, VALVANO MA, HOLST O, KNIREL YA, QI Y, JO S, KLAUDA JB, WIDMALM G & IM W 2018. CHARMM-GUI Membrane Builder for Complex Biological Membrane Simulations with Glycolipids and Lipoglycans. Journal of Chemical Theory and Computation, 15, 775–786. [PubMed: 30525595]

LIEBSCHNER D, AFONINE PV, BAKER ML, BUNKÓCZI G, CHEN VB, CROLL TI, HINTZE B, HUNG L-W, JAIN S, MCCOY AJ, MORIARTY NW, OEFFNER RD, POON BK, PRISANT MG, READ RJ, RICHARDSON JS, RICHARDSON DC, SAMMITO MD, SOBOLEV OV, STOCKWELL DH, TERWILLIGER TC, URZHUMTSEV AG, VIDEAU LL, WILLIAMS CJ & ADAMS PD 2019. Macromolecular structure determination using X-rays, neutrons and electrons: recent developments in Phenix. Acta Crystallographica. Section D, Structural Biology, 75, 861–877. [PubMed: 31588918]

LIU J-L, YEE C, WANG Y & HEKIMI S 2017. A single biochemical activity underlies the pleiotropy of the aging-related protein CLK-1. Scientific Reports, 7, 859. [PubMed: 28404998]

LIU M & LU S 2016. Plastoquinone and Ubiquinone in Plants: Biosynthesis, Physiological Function and Metabolic Engineering. Frontiers in Plant Science, 7, 1898. [PubMed: 28018418]

LOHMAN DC, AYDIN D, BANK HCV, SMITH RW, LINKE V, WEISENHORN E, MCDEVITT MT, HUTCHINS P, WILKERSON EM, WANCEWICZ B, RUSSELL J, STEFELY MS, BEEBE ET, JOCHEM A, COON JJ, BINGMAN CA, PERARO MD & PAGLIARINI DJ 2019. An Isoprene Lipid-Binding Protein Promotes Eukaryotic Coenzyme Q Biosynthesis. Molecular Cell, 73, 763–774.e10. [PubMed: 30661980]

LOHMAN DC, FOROUHAR F, BEEBE ET, STEFELY MS, MINOGUE CE, ULBRICH A, STEFELY JA, SUKUMAR S, LUNA-SÁNCHEZ M, JOCHEM A, LEW S, SEETHARAMAN J, XIAO R, WANG H, WESTPHALL MS, WROBEL RL, EVERETT JK, MITCHELL JC, LÓPEZ LC, COON JJ, TONG L & PAGLIARINI DJ 2014. Mitochondrial COQ9 is a lipid-binding protein that associates with COQ7 to enable coenzyme Q biosynthesis. Proceedings of the National Academy of Sciences, 111, E4697–E4705.

LU T-T, LEE SJ, APFEL U-P & LIPPARD SJ 2013. Aging-Associated Enzyme Human Clock-1: Substrate-Mediated Reduction of the Diiron Center for 5-Demethoxyubiquinone Hydroxylation. Biochemistry, 52, 2236–2244. [PubMed: 23445365]

MARBOIS B, GIN P, FAULL KF, POON WW, LEE PT, STRAHAN J, SHEPHERD JN & CLARKE CF 2005. Coq3 and Coq4 Define a Polypeptide Complex in Yeast Mitochondria for the Biosynthesis of Coenzyme Q*. Journal of Biological Chemistry, 280, 20231–20238. [PubMed: 15792955]

MARBOIS B, GIN P, GULMEZIAN M & CLARKE CF 2009. The yeast Coq4 polypeptide organizes a mitochondrial protein complex essential for coenzyme Q biosynthesis. Biochimica et Biophysica Acta (BBA) - Molecular and Cell Biology of Lipids, 1791, 69–75. [PubMed: 19022396]

MASTRONARDE DN 2005. Automated electron microscope tomography using robust prediction of specimen movements. Journal of Structural Biology, 152, 36–51. [PubMed: 16182563]

MATYASH V, LIEBISCH G, KURZCHALIA TV, SHEVCHENKO A & SCHWUDKE D 2008. Lipid extraction by methyl-tert-butyl ether for high-throughput lipidomics. J Lipid Res, 49, 1137–46. [PubMed: 18281723]

METZ G, HOWARD KP, VANLIEMT WBS, PRESTEGARD JH, LUGTENBURG J & SMITH SO 1995. Nmr-Studies of Ubiquinone Location in Oriented Model Membranes - Evidence for a Single Motionally-Averaged Population. Journal of the American Chemical Society, 117, 564–565.

MICHAELIS L & MOORE MJ 1985. Location of ubiquinone-10 (CoQ-10) in phospholipid vesicles. Biochimica et Biophysica Acta (BBA) - Biomembranes, 821, 121–129. [PubMed: 4063355]

MONAGHAN RM, BARNES RG, FISHER K, ANDREOU T, ROONEY N, POULIN GB & WHITMARSH AJ 2015. A nuclear role for the respiratory enzyme CLK-1 in regulating mitochondrial stress responses and longevity. Nature Cell Biology, 17, 782–792. [PubMed: 25961505]

MOORE AL, SHIBA T, YOUNG L, HARADA S, KITA K & ITO K 2013. Unraveling the Heater: New Insights into the Structure of the Alternative Oxidase. Annual Review of Plant Biology, 64, 637–663.

MOREIN S, ANDERSSON A-S, RILFORS L & LINDBLOM G 1996. Wild-type Escherichia coli Cells Regulate the Membrane Lipid Composition in a “Window” between Gel and Non-lamellar Structures (∗). Journal of Biological Chemistry, 271, 6801–6809. [PubMed: 8636103]

MORGENSTERN M, STILLER SB, LÜBBERT P, PEIKERT CD, DANNENMAIER S, DREPPER F, WEILL U, HÖß P, FEUERSTEIN R, GEBERT M, BOHNERT M, LAAN MVD, SCHULDINER M, SCHÜTZE C, OELJEKLAUS S, PFANNER N, WIEDEMANN N & WARSCHEID B 2017. Definition of a High-Confidence Mitochondrial Proteome at Quantitative Scale. Cell Reports, 19, 2836–2852. [PubMed: 28658629]

MOSER CC, KESKE JM, WARNCKE K, FARID RS & DUTTON PL 1992. Nature of biological electron transfer. Nature, 355, 796–802. [PubMed: 1311417]

NOWICKA B & KRUK J 2010. Occurrence, biosynthesis and function of isoprenoid quinones. Biochimica et Biophysica Acta (BBA) - Bioenergetics, 1797, 1587–1605. [PubMed: 20599680]

OLGAC A, ÖZTOPRAK Ü, KASAPKARA ÇS, KıLıÇ M, YÜKSEL D, DERINKUYU EB, YıLDıZ YT, CEYLANER S & EZGU FS 2020. A rare case of primary coenzyme Q10 deficiency due to COQ9 mutation. Journal of Pediatric Endocrinology and Metabolism, 33, 165–170. [PubMed: 31821167]

PADILLA S, TRAN UC, JIMÉNEZ-HIDALGO M, LÓPEZ-MARTÍN JM, MARTÍN-MONTALVO A, CLARKE CF, NAVAS P & SANTOS-OCAÑA C 2008. Hydroxylation of demethoxy-Q6 constitutes a control point in yeast coenzyme Q6 biosynthesis. Cellular and Molecular Life Sciences, 66, 173.

PAVELITES JJ, GAO J, BASH PA & MACKERELL AD 1997. A molecular mechanics force field for NAD+ NADH, and the pyrophosphate groups of nucleotides. Journal of Computational Chemistry, 18, 221–239.

PETTERSEN EF, GODDARD TD, HUANG CC, COUCH GS, GREENBLATT DM, MENG EC & FERRIN TE 2004. UCSF Chimera—A visualization system for exploratory research and analysis. Journal of Computational Chemistry, 25, 1605–1612. [PubMed: 15264254]

PRAVDA L, SEHNAL D, TOUŠEK D, NAVRÁTILOVÁ V, BAZGIER V, BERKA K, VAŘEKOVÁ RS, KOČA J & OTYEPKA M 2018. MOLEonline: a web-based tool for analyzing channels, tunnels and pores (2018 update). Nucleic Acids Research, 46, W368–W373. [PubMed: 29718451]

PUNJANI A, RUBINSTEIN JL, FLEET DJ & BRUBAKER MA 2017. cryoSPARC: algorithms for rapid unsupervised cryo-EM structure determination. Nature Methods, 14, 290–296. [PubMed: 28165473]

REINER S, MICOLOD D, ZELLNIG G & SCHNEITER R 2006. A Genomewide Screen Reveals a Role of Mitochondria in Anaerobic Uptake of Sterols in Yeast. Molecular Biology of the Cell, 17, 90–103. [PubMed: 16251356]

ROHOU A & GRIGORIEFF N 2015. CTFFIND4: Fast and accurate defocus estimation from electron micrographs. Journal of Structural Biology, 192, 216–221. [PubMed: 26278980]

SAMORÌ B, LENAZ G, BATTINO M, MARCONI G & DOMINI I 1992. On coenzyme Q orientation in membranes: A linear dichroism study of ubiquinones in a model bilayer. The Journal of Membrane Biology, 128, 193–203. [PubMed: 1501247]

SCHNEIDER CA, RASBAND WS & ELICEIRI KW 2012. NIH Image to ImageJ: 25 years of image analysis. Nature Methods, 9, 671–675. [PubMed: 22930834]

SCHOEPP-COTHENET B, VAN LIS R, ATTEIA A, BAYMANN F, CAPOWIEZ L, DUCLUZEAU AL, DUVAL S, TEN BRINK F, RUSSELL MJ & NITSCHKE W 2013. On the universal core of bioenergetics. Biochim Biophys Acta, 1827, 79–93. [PubMed: 22982447]

SINGHAROY A, MAFFEO C, DELGADO-MAGNERO KH, SWAINSBURY DJK, SENER M, KLEINEKATHÖFER U, VANT JW, NGUYEN J, HITCHCOCK A, ISRALEWITZ B, TEO I, CHANDLER DE, STONE JE, PHILLIPS JC, POGORELOV TV, MALLUS MI, CHIPOT C, LUTHEY-SCHULTEN Z, TIELEMAN DP, HUNTER CN, TAJKHORSHID E, AKSIMENTIEV A & SCHULTEN K 2019. Atoms to Phenotypes: Molecular Design Principles of Cellular Energy Metabolism. Cell, 179, 1098–1111.e23. [PubMed: 31730852]

SMITH AC, ITO Y, AHMED A, SCHWARTZENTRUBER JA, BEAULIEU CL, ABERG E, MAJEWSKI J, BULMAN DE, HORSTING-WETHLY K, KONING DVD, CONSORTIUM CRC, RODENBURG RJ, BOYCOTT KM & PENNEY LS 2018. A family segregating lethal neonatal coenzyme Q10 deficiency caused by mutations in COQ9. Journal of Inherited Metabolic Disease, 41, 719–729. [PubMed: 29560582]

SOHLENKAMP C & GEIGER O 2016. Bacterial membrane lipids: diversity in structures and pathways. FEMS Microbiology Reviews, 40, 133–159. [PubMed: 25862689]

STEFELY JA & PAGLIARINI DJ 2017. Biochemistry of Mitochondrial Coenzyme Q Biosynthesis. Trends in Biochemical Sciences, 42, 824–843. [PubMed: 28927698]

SUBRAMANIAN K, JOCHEM A, VASSEUR ML, LEWIS S, PAULSON BR, REDDY TR, RUSSELL JD, COON JJ, PAGLIARINI DJ & NUNNARI J 2019. Coenzyme Q biosynthetic proteins assemble in a substrate-dependent manner into domains at ER–mitochondria contacts. Journal of Cell Biology, 218, 1353–1369. [PubMed: 30674579]

SZKLARCZYK D, GABLE AL, NASTOU KC, LYON D, KIRSCH R, PYYSALO S, DONCHEVA NT, LEGEAY M, FANG T, BORK P, JENSEN LJ & VON MERING C 2020. The STRING database in 2021: customizable protein–protein networks, and functional characterization of user-uploaded gene/measurement sets. Nucleic Acids Research, 49, gkaa1074–.

TAUCHE A, KRAUSE-BUCHHOLZ U & RÖDEL G 2008. Ubiquinone biosynthesis in Saccharomyces cerevisiae: the molecular organization of O-methylase Coq3p depends on Abc1p/Coq8p. FEMS Yeast Research, 8, 1263–1275. [PubMed: 18801050]

TEIXEIRA MH & ARANTES GM 2019. Effects of lipid composition on membrane distribution and permeability of natural quinones. RSC Advances, 9, 16892–16899. [PubMed: 35516391]

TRAN UC, MARBOIS B, GIN P, GULMEZIAN M, JONASSEN T & CLARKE CF 2006. Complementation of Saccharomyces cerevisiae coq7 Mutants by Mitochondrial Targeting of the Escherichia coli UbiF Polypeptide TWO FUNCTIONS OF YEAST COQ7 POLYPEPTIDE IN COENZYME Q BIOSYNTHESIS* * This work was supported by National Institutes of Health Grant GM45952. The costs of publication of this article were defrayed in part by the payment of page charges. This article must therefore be hereby marked “advertisement” in accordance with 18 U.S.C. Section 1734 solely to indicate this fact. Journal of Biological Chemistry, 281, 16401–16409. [PubMed: 16624818]

TURUNEN M, OLSSON J & DALLNER G 2004. Metabolism and function of coenzyme Q. Biochimica et Biophysica Acta (BBA) - Biomembranes, 1660, 171–199. [PubMed: 14757233]

VANOMMESLAEGHE K, HATCHER E, ACHARYA C, KUNDU S, ZHONG S, SHIM J, DARIAN E, GUVENCH O, LOPES P, VOROBYOV I & MACKERELL AD JR. 2010. CHARMM general force field: A force field for drug-like molecules compatible with the CHARMM all-atom additive biological force fields. J Comput Chem, 31, 671–90. [PubMed: 19575467]

VANOMMESLAEGHE K & MACKERELL AD JR. 2012. Automation of the CHARMM General Force Field (CGenFF) I: bond perception and atom typing. J Chem Inf Model, 52, 3144–54. [PubMed: 23146088]

VÖGTLE FN, BURKHART JM, GONCZAROWSKA-JORGE H, KÜCÜKKÖSE C, TASKIN AA, KOPCZYNSKI D, AHRENDS R, MOSSMANN D, SICKMANN A, ZAHEDI RP & MEISINGER C 2017. Landscape of submitochondrial protein distribution. Nature Communications, 8, 290.

VÖGTLE FN, BURKHART JM, RAO S, GERBETH C, HINRICHS J, MARTINOU J-C, CHACINSKA A, SICKMANN A, ZAHEDI RP & MEISINGER C 2012. Intermembrane Space Proteome of Yeast Mitochondria*. Molecular & Cellular Proteomics : MCP, 11, 1840–1852. [PubMed: 22984289]

WANG Y, GUMUS E & HEKIMI S 2022. A novel COQ7 mutation causing primarily neuromuscular pathology and its treatment options. Mol Genet Metab Rep, 31, 100877. [PubMed: 35782625]

WANG Y & HEKIMI S 2021. Minimal mitochondrial respiration is required to prevent cell death by inhibition of mTOR signaling in CoQ-deficient cells. Cell Death Discovery, 7, 201. [PubMed: 34349107]

WANG Y, OXER D & HEKIMI S 2015. Mitochondrial function and lifespan of mice with controlled ubiquinone biosynthesis. Nature Communications, 6, 6393.

WANG Y, SMITH C, PARBOOSINGH JS, KHAN A, INNES M & HEKIMI S 2017. Pathogenicity of two COQ7 mutations and responses to 2,4-dihydroxybenzoate bypass treatment. Journal of Cellular and Molecular Medicine, 21, 2329–2343. [PubMed: 28409910]

WILLIAMS CJ, HEADD JJ, MORIARTY NW, PRISANT MG, VIDEAU LL, DEIS LN, VERMA V, KEEDY DA, HINTZE BJ, CHEN VB, JAIN S, LEWIS SM, ARENDALL WB, SNOEYINK J, ADAMS PD, LOVELL SC, RICHARDSON JS & RICHARDSON DC 2018. MolProbity: More and better reference data for improved all-atom structure validation. Protein Science, 27, 293–315. [PubMed: 29067766]

YEN H-C, YEH W-Y, LEE S-H, FENG Y-H & YANG S-L 2020. Characterization of human mitochondrial PDSS and COQ proteins and their roles in maintaining coenzyme Q10 levels and each other's stability. Biochimica et Biophysica Acta (BBA) - Bioenergetics, 1861, 148192. [PubMed: 32194061]

ZHANG K 2016. Gctf: Real-time CTF determination and correction. Journal of Structural Biology, 193, 1–12. [PubMed: 26592709]

ZHENG SQ, PALOVCAK E, ARMACHE J-P, VERBA KA, CHENG Y & AGARD DA 2017. MotionCor2: anisotropic correction of beam-induced motion for improved cryo-electron microscopy. Nature Methods, 14, 331–332. [PubMed: 28250466]

ZIVANOV J, NAKANE T, FORSBERG BO, KIMANIUS D, HAGEN WJH, LINDAHL E & SCHERES SHW 2018. New tools for automated high-resolution cryo-EM structure determination in RELION-3. eLife, 7, e42166. [PubMed: 30412051]

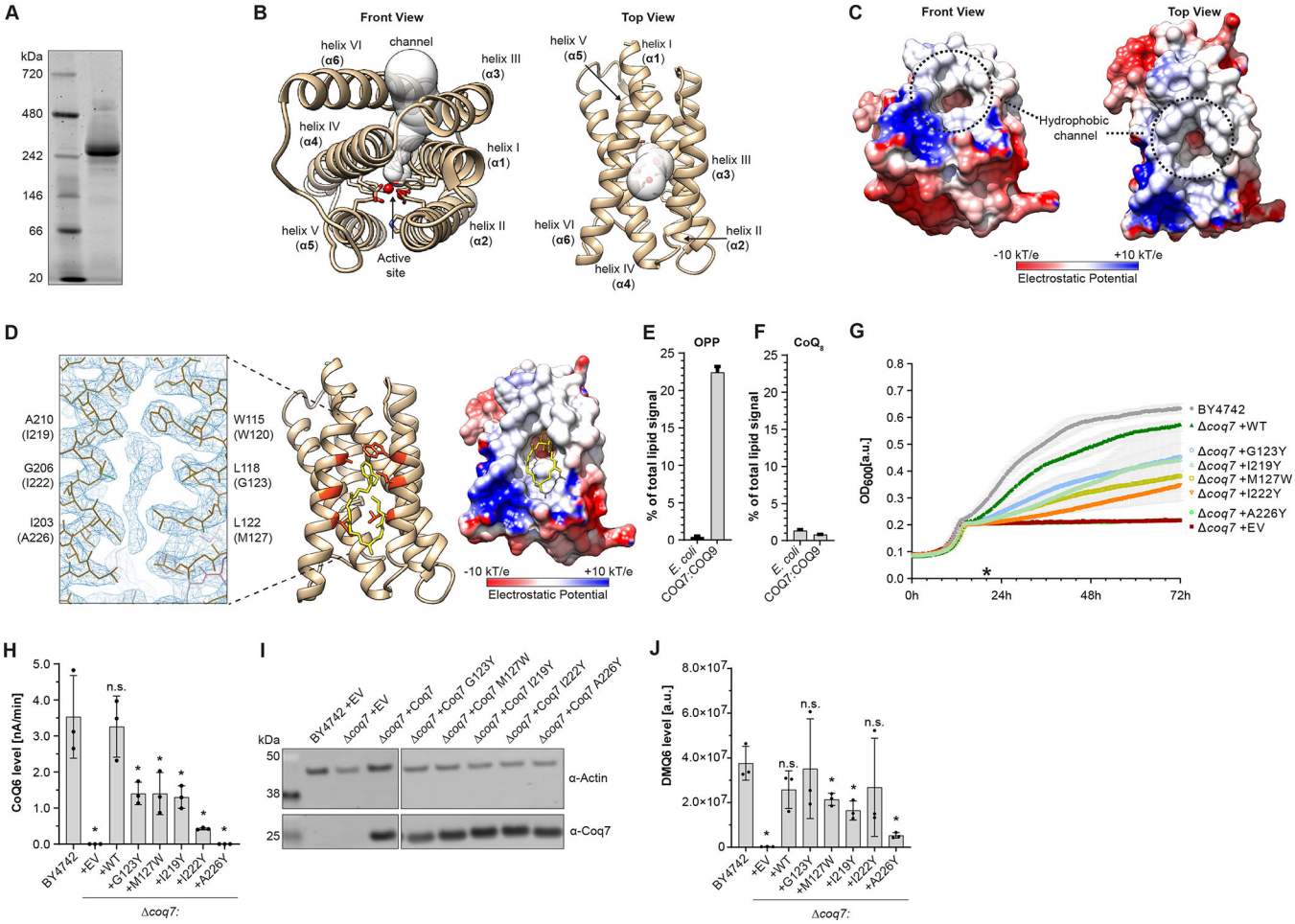


**Figure 1. Structure – function characterization of COQ7.**

(A) Native PAGE analysis of purified GB1-$^{Nd38}$COQ7:His6-$^{Nd79}$COQ9 complex.

(B) Structure of COQ7 with visible channel leading to an active site. Iron atoms were not resolved by cryo-EM and were added based on the structure of bactoferritin (PDB:4AM2).

(C) Electrostatic surface potential of COQ7 with visible entry to the hydrophobic channel.

(D) The hydrophobic channel with visible additional ligand density inside. Important residues are labeled. Corresponding residues in yeast are in parentheses.

(E,F) Octaprenylphenol (OPP) and Coenzyme $Q_8$ ($CoQ_8$) in *E. coli* cells and the GB1-$^{Nd38}$COQ7:His6-$^{Nd79}$COQ9 complex purified from *E. coli*. (mean ± s.d., $n = 2$).

(G) Growth of Coq7 mutants. Cells start with fermentation and then switch to respiration (mean ± s.d., $n = 3$). (*) corresponds to time point used for measurements in panel H,I,J.

(H) Coenzyme $Q_6$ level in Coq7 mutants (mean ± s.d., $n = 3$, one-sided Student's *t*-test, *p<0.05, n.s. not significant).

(I) Expression level of the Coq7 yeast mutants. Native Coq7 in BY4742 strain is below the limit of detection.

(J) $DMQ_6$ level in Coq7 mutants. (mean ± s.d., $n = 3$, one-sided Student's *t*-test, *p<0.05, n.s. not significant).

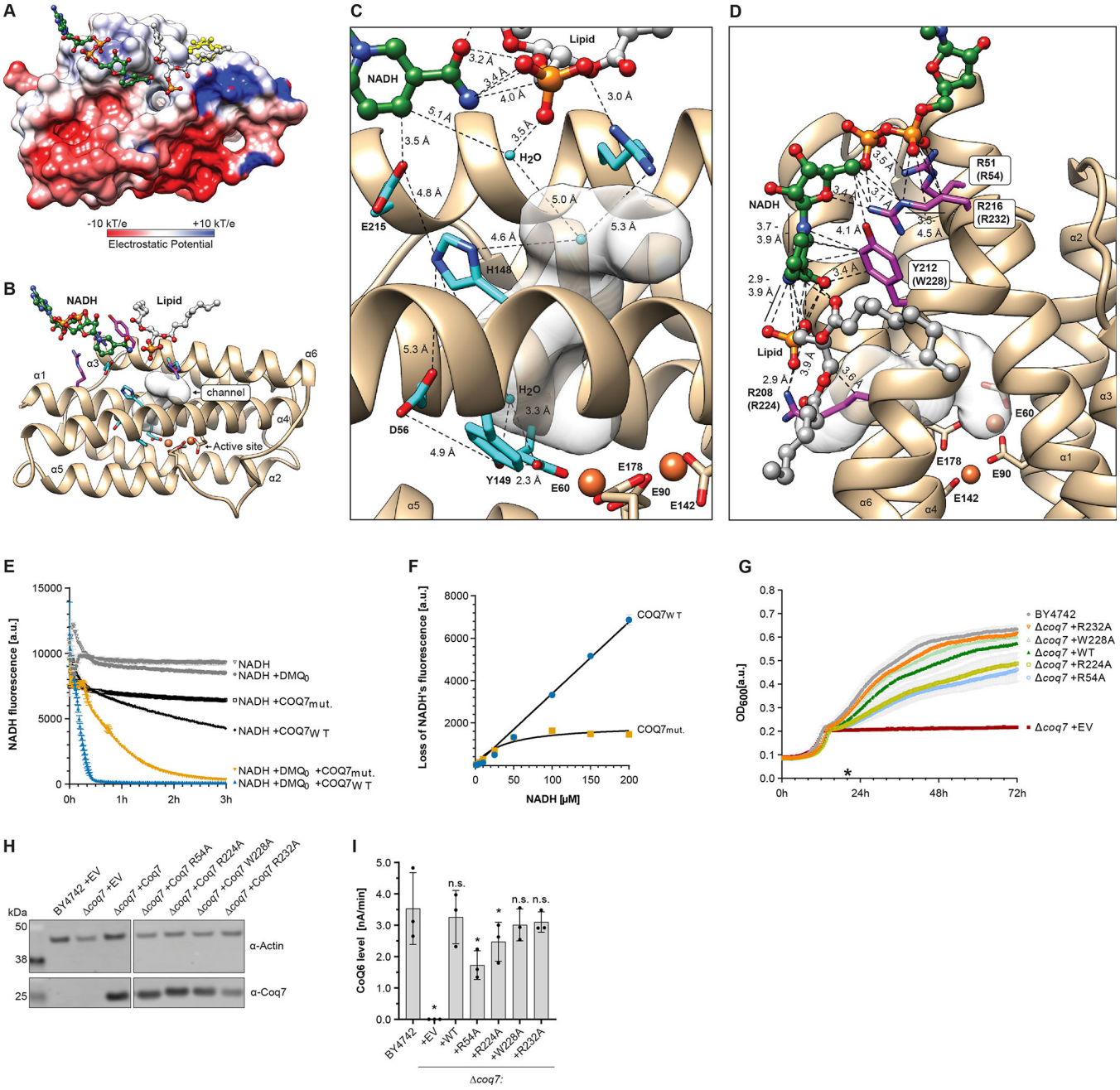


**Figure 2. Details of NADH binding to COQ7.**

(A) Electrostatic surface potential of COQ7 with bound NADH molecule (green) and OPP (yellow).

(B) Ribbon view of COQ7's NADH binding site and channel leading to the active site.

(C) Structural elements that might participate in charge transfer from NADH to COQ7.

(D) Details of NADH binding by conserved arginines and tyrosine. Corresponding residues in yeast are in parentheses.

(E) NADH oxidation *in vitro* assay showing activities of WT and RRYR/AAAA COQ7 mutant (mean ± s.d., $n = 3$).

(F) Effect of the RRYR/AAAA mutation as a function of NADH concentration. The graph shows 30 min. time point extracted from data presented in Figure S9G, S9H (mean ± s.d., $n$ = 3).

(G) Growth Coq7 mutants. Cells start with fermentation and then switch to respiration(mean ± s.d., $n$ = 3). (*) corresponds to time point used for measurements in panels H,I.

(H) Expression level of the Coq7 yeast mutants.. Native Coq7 in BY4742 strain is below the limit of detection.

(I) Coenzyme $Q_6$ ($CoQ_6$) level in Coq7 mutants. (mean ± s.d., $n$ = 3, one-sided Student's $t$-test, *p<0.05, n.s. not significant).

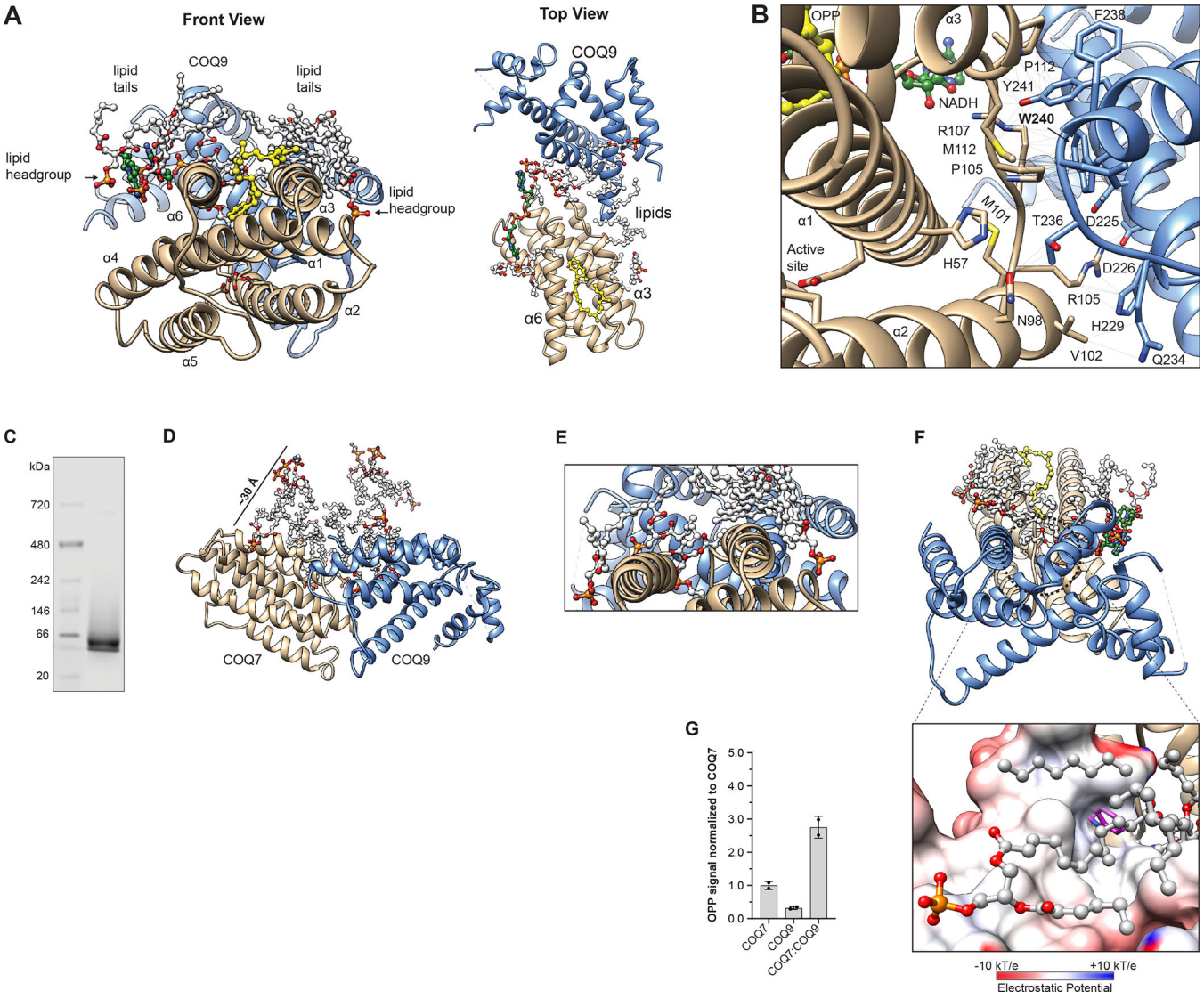


**Figure 3. Structure of COQ7:COQ9 heterodimer in lipid environment.**

(A) Snapshot of the COQ7:COQ9 heterodimer structure with visible lipids (light gray), NADH (green) and OPP (yellow).

(B) Details of the COQ7:COQ9 interaction interface.

(C) Native Page of the GB1-$^{Nd38}$COQ7:His6-$^{Nd79}$COQ9$^{W240K}$ complex.

(D) Zoom on lipid molecules forming a lipid pseudo-bilayer.

(E) Zoom on the tilted lipid headgroups (orange and red).

(F) Zoom on lipid-binding substrate pocket in COQ9 surrounded by surface lipids. No quinone density is detected around the substrate-binding COQ9's W240 residue (magenta).

(G) LC-MS lipidomic analysis of OPP content in individually purified His6-GB1-$^{Nd38}$COQ7, His6-$^{Nd79}$COQ9 or the full GB1-$^{Nd38}$COQ7:His6-$^{Nd79}$COQ9 complex (mean ± s.d., $n = 2$).

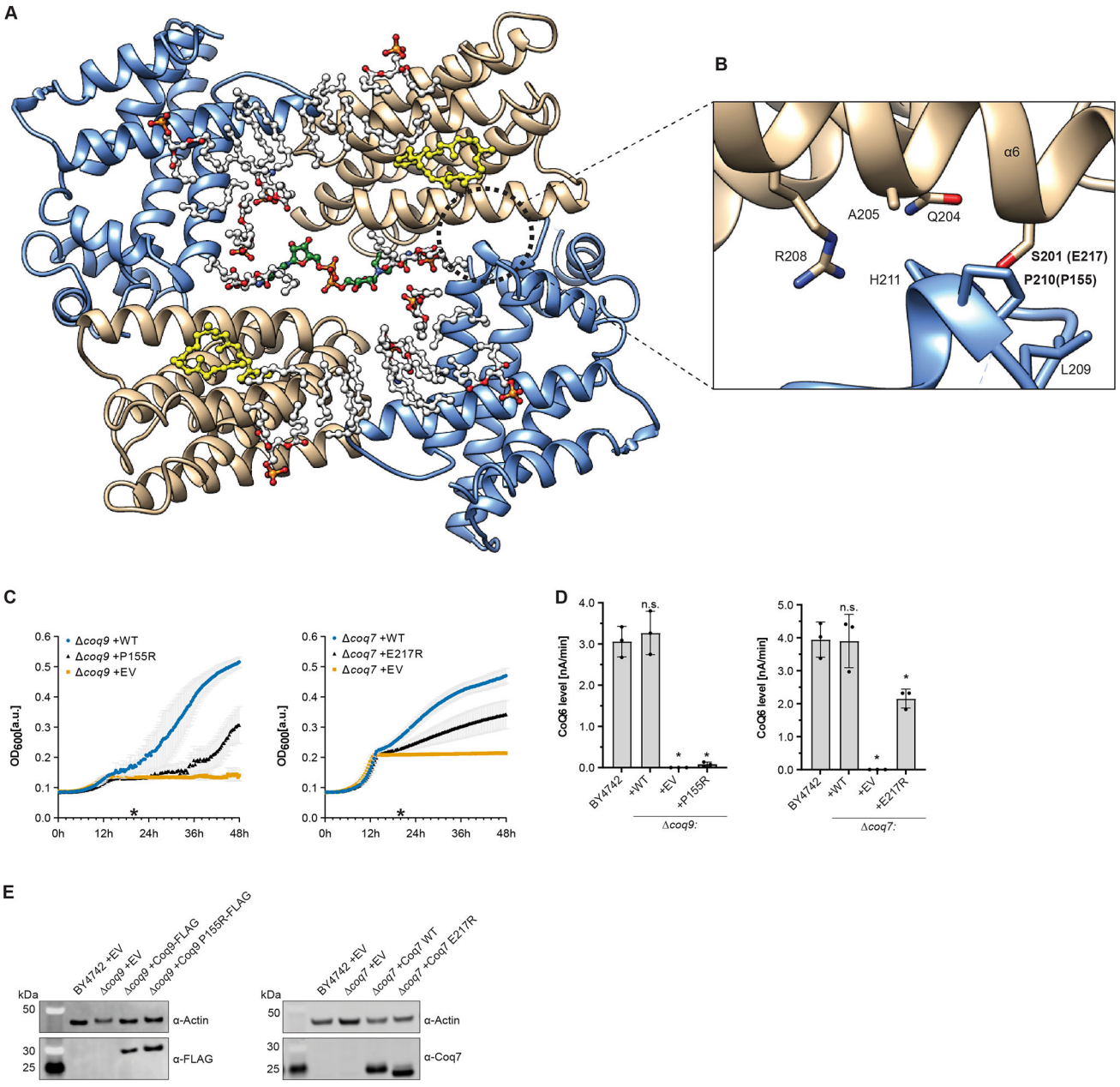


**Figure 4. Structure of the COQ7:COQ9 heterotetramer.**

(A) Membrane view of one COQ7:COQ9 tetramer.

(B) Details of COQ7:COQ9 interaction mediating tetramer's formation. COQ9 P210 and COQ7 S201 residues are labeled in bold and their corresponding residues in yeast are provided in parentheses.

(C) Respiratory growth of Coq7 or Coq9 mutants. Cells start with fermentation and then switch to respiration.(mean ± s.d., $n = 3$). (*) corresponds to time point used for measurements in panel D,E.

(D) Coenzyme $Q_6$ level in Coq7 or Coq9 mutant (mean ± s.d., $n = 3$, one-sided Student's $t$-test, *p<0.05, n.s. not significant).

(E) Expression level of the Coq7 or Coq9 yeast mutants (TEF promoter Native Coq7 in BY4742 strain is below the limit of detection.

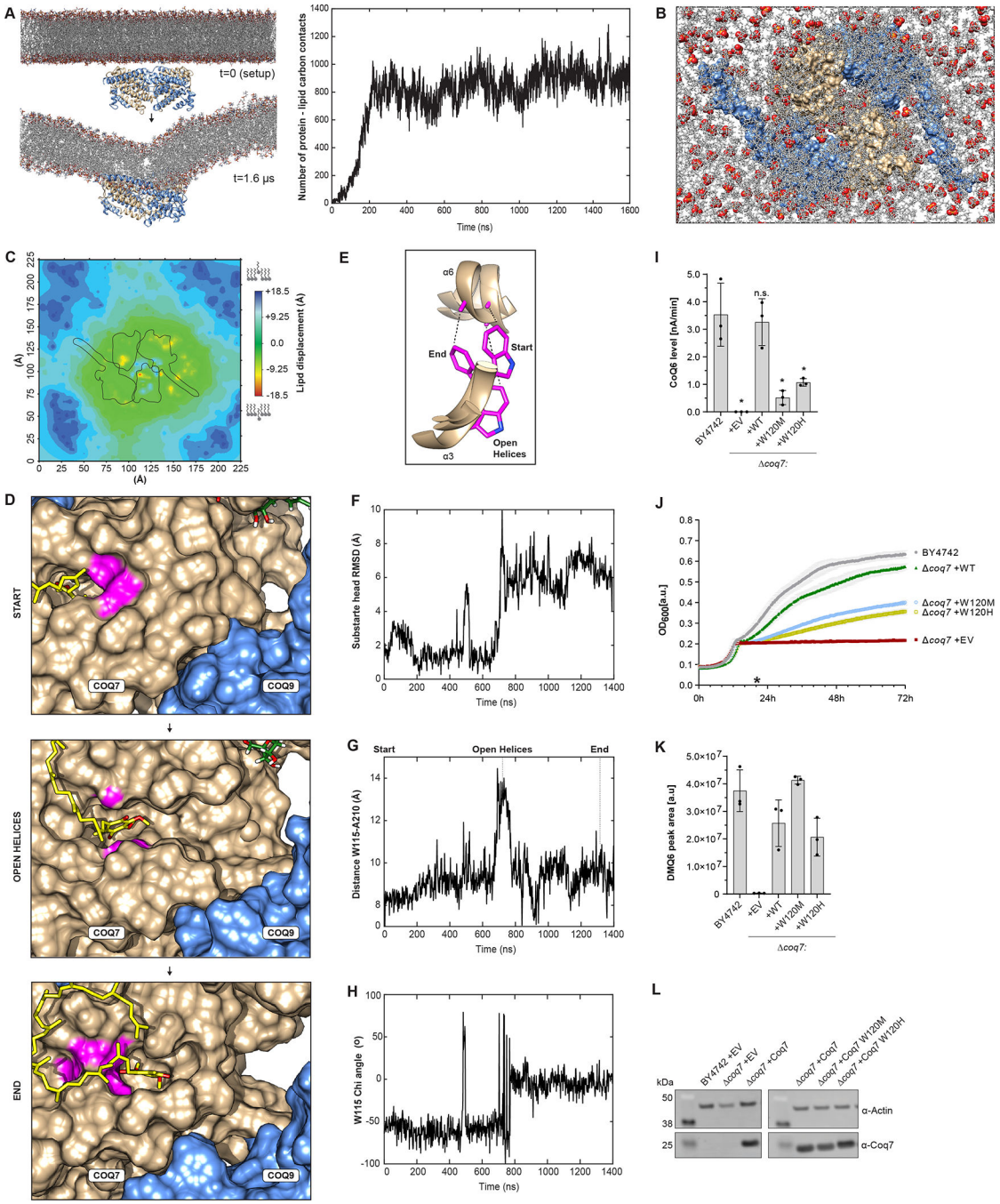


**Figure 5. MD simulations of the COQ7:COQ9 tetramer at the membrane.**

(A) Membrane binding and deformation observed in the atomistic MD simulations. The graph describes the number of non-hydrogen atom-atom contacts within 5 Å cutoff between COQ7 or COQ9 and the carbon tails of the lipids over time.

(B) Shot of the protein-membrane complex observed after 1.6 μs of simulation. Phosphate groups representing lipid headgroups are displayed as red spheres. Other atoms are displayed as sticks. COQ7 (tan) and COQ9 (blue) are visible as surfaces.

(C) Map of the deformation of the bottom membrane leaflet induced by the proteins binding to it.
(D) Snapshots from molecular dynamics simulation at 450 K showing release of $CoQ_{10}$ from COQ7 (tan) towards COQ9 (blue) by gating through W115 and A210 (magenta).
(E) Overlaid positions of the gating W115 and A210 residues from COQ7 conformations visible in panel D.
(F) R.M.S.D. of the $CoQ_{10}$ head group as a proxy for its displacement out of the active site.
(G) Time plot showing the distance between the Cα atoms of W115 and A210.
(H) Time plot showing the sidechain torsion angle of W115.
(I) Coenzyme $Q_6$ ($CoQ_6$) level in Coq7 mutants (mean ± s.d., $n = 3$, one-sided Student's $t$-test, *p<0.05, n.s. not significant).
(J) Growth of Coq7 mutants. Cells start with fermentation and then switch to respiration (mean ± s.d., $n = 3$).(*) corresponds to time point used for measurements in panels I,J,L.
(K) $DMQ_6$ level in Coq7 mutants. (mean ± s.d., $n = 3$, one-sided Student's $t$-test, *p<0.05, n.s. not significant).
(L) Expression level of the Coq7 yeast mutants. Native Coq7 in BY4742 strain is below the limit of detection.

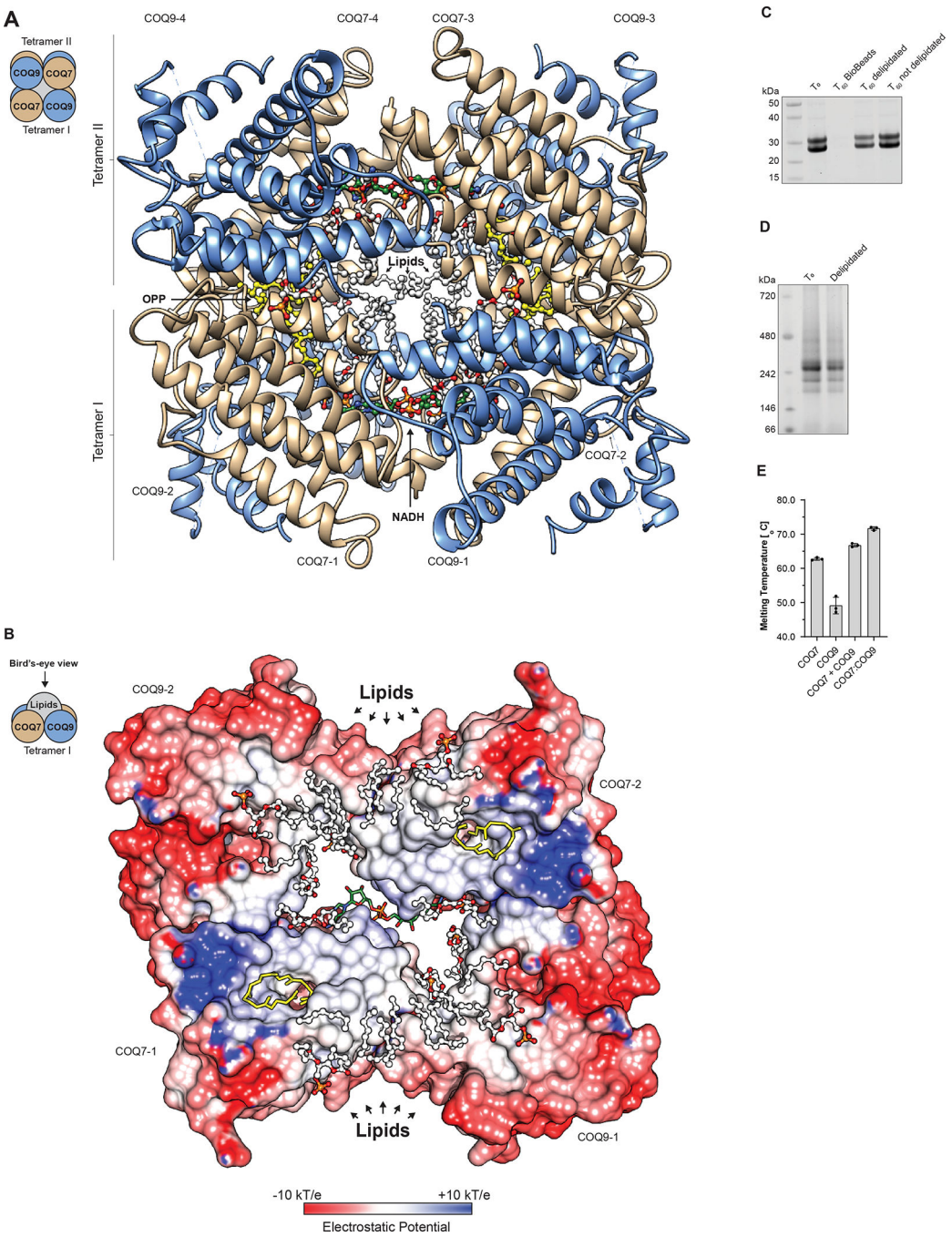


**Figure 6. Two COQ7:COQ9 tetramers form an octamer.(**

A) Structure of the octamer with visible bound lipids (white), NADH (green) and OPP (yellow).

(B) Hydrophobic interior of the octamer displayed as electrostatic surface of one of the COQ7:COQ9 tetramers. Stabilizing lipids (white), NADH (green) and OPP (yellow) shown.

(C) SDS-PAGE analysis of protein stability upon delipidation of the GB1-$^{Nd38}$COQ7:His6-$^{Nd79}$COQ9 with BioBeads; $T_0$ – soluble fraction before delipidation, $T_{60}$ BioBeads – protein bound to beads after 60 min. incubation, $T_{60}$ delipidated – soluble fraction after

60 min. delipidation, $T_{60}$ not delipidated – soluble fraction after 60 min. incubation without BioBeads.

(D) Native PAGE analysis of the GB1-$^{Nd38}$COQ7:His6-$^{Nd79}$COQ9 complex after 1h . delipidation.

(E) DSF analysis of melting temperatures of individually purified His6-$^{Nd38}$COQ7, His6-$^{Nd79}$COQ9, their mix and the GB1-$^{Nd38}$COQ7:His6-$^{Nd79}$COQ9 complex.

**Table 1.**

Cryo-EM data collection, refinement, and validation statistics.

| | NADH-bound COQ7:COQ9 complex (EMD-25413) (PDB 7SSS) | COQ7:COQ9 complex only (EMD-25412) (PDB 7SSP) |
|---|---|---|
| **Data collection and processing** | | |
| Microscope | FEI Titan Krios | FEI Talos Arctica |
| Camera | Gatan K3 Summit | Gatan K3 Summit |
| Magnification | 105,000x | 36,000x |
| Voltage (kV) | 300 | 200 |
| Electron exposure ($e^{-}$/Å$^2$) | 65 | 58.8 |
| Defocus (μm) | −0.3 to −1.2 | −0.5 to −1.5 |
| Pixel size (Å) | 0.833 | 1.14 |
| Symmetry imposed | D2 | D2 |
| Micrographs (no.) | 10,088 | 1,395 |
| Initial particle images (no.) | 2,709,398 | 574,760 |
| Final particle images (no.) | 372,917 | 61,526 |
| Map resolution (Å) | 2.4 | 3.5 |
| FSC threshold | 0.143 | 0.143 |
| Map resolution range (Å) | 2.2 to 6.7 | 3.4 to 5.9 |
| | | |
| **Refinement** | | |
| Initial model used (PDB code) | COQ7 (*de novo*) – COQ9 (6AWL) | COQ7 (*de novo*) – COQ9 (6AWL) |
| Model resolution (Å) | 2.4 | 3.5 |
| FSC threshold | 0.143 | 0.143 |
| Map sharpening *B* factor (Å$^2$) | −95.99 | −156.07 |
| Model composition | | |
| Nonhydrogen atoms | 12,190 | 10,930 |
| Protein residues | 1,416 | 1,376 |
| Ligands | 4 | |
| Lipids | 32 | |
| Cofactor | 2 | |
| Water | 170 | |
| B factors (Å$^2$) | | |
| Protein | 25.11 | 22.16 |
| Ligands | 43.18 | |
| Water | 30.84 | |
| R.m.s. deviations | | |
| Bond lengths (Å) | 0.004 | 0.004 |
| Bond angles (Å) | 0.449 | 0.611 |
| **Validation** | | |

| | NADH-bound COQ7:COQ9 complex (EMD-25413) (PDB 7SSS) | COQ7:COQ9 complex only (EMD-25412) (PDB 7SSP) |
|---|---|---|
| MolProbity score | 1.27 | 1.67 |
| Clashscore | 4.01 | 4.52 |
| Poor rotamers (%) | 0.0 | 0.0 |
| Ramachandran plot | | |
| Favored (%) | 97.63 | 93.15 |
| Allowed (%) | 2.37 | 6.85 |
| Disallowed (%) | 0.0 | 0.0 |